Cell Reports

Resource

Microglia-astrocyte crosstalk in the amyloid plaque niche of an Alzheimer's disease mouse model, as revealed by spatial transcriptomics

Graphical abstract

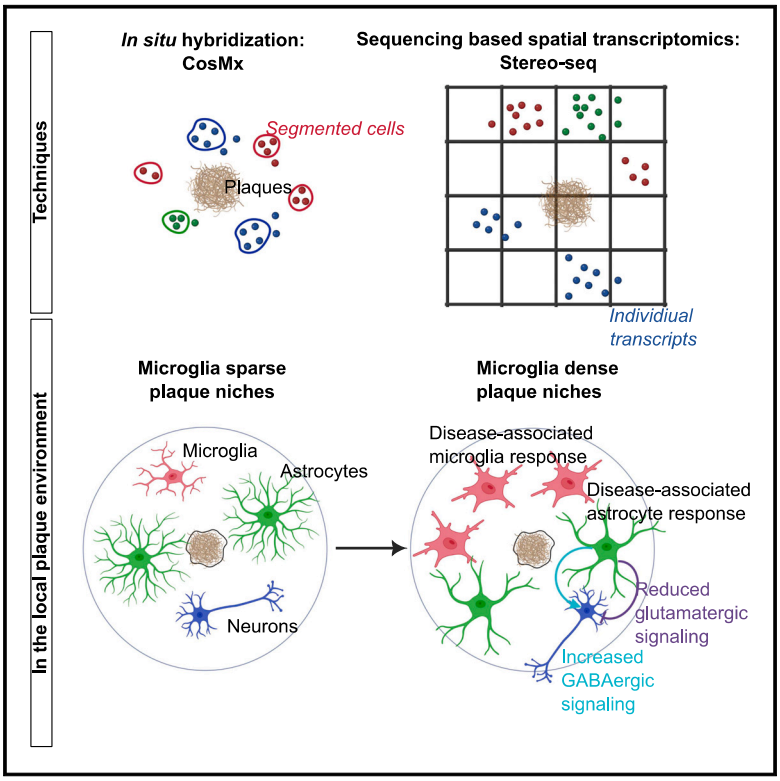

Authors

Anna Mallach, Magdalena Zielonka, Veerle van Lieshout, ..., I. Lorena Arancibia-Carcamo, Mark Fiers, Bart De Strooper

Correspondence

mark.fiers@kuleuven.be (M.F.), b.strooper@ukdri.ac.uk (B.D.S.)

In brief

Mallach et al. resolve the local environment around amyloid pathology in mice. Next to microglia, astrocytes emerge as a key signaling partner in this disease environment, interacting with both microglia and neurons. By interrogating signaling pathways, this study highlights the role activated astrocytes play in disrupting neuronal signaling.

Highlights

- The microglial response to plaques is consistent across different brain regions
- The local neighborhood of amyloid plaques demonstrates heterogeneous compositions
- Astrocytes in microglia-dense plaque niches acquire a more neurotoxic signature
- Activated astrocytes appear to disrupt neuronal signaling

Mallach et al., 2024, Cell Reports *43*, 114216
June 25, 2024
https://doi.org/10.1016/j.celrep.2024.114216

CellPress

Cell Reports

CellPress
OPEN ACCESS

Resource

Microglia-astrocyte crosstalk in the amyloid plaque niche of an Alzheimer's disease mouse model, as revealed by spatial transcriptomics

Anna Mallach,[1,2,3,8] Magdalena Zielonka,[3,4,8] Veerle van Lieshout,[3,4] Yanru An,[5] Jia Hui Khoo,[5] Marisa Vanheusden,[3,4,6] Wei-Ting Chen,[3,4,6] Daan Moechars,[3,4] I. Lorena Arancibia-Carcamo,[1,2] Mark Fiers,[1,2,3,4,7,*] and Bart De Strooper[1,2,3,4,9,*]

[1]UK Dementia Research Institute at UCL, University College London, London WC1E 6BT, UK
[2]The Francis Crick Institute, London NW1 1AT, UK
[3]Department of Neurosciences and Leuven Brain Institute, KU Leuven, Leuven, Belgium
[4]Laboratory for the Research of Neurodegenerative Diseases, VIB Center for Brain & Disease Research, VIB, Leuven, Belgium
[5]BGI Research, 49276 Riga, Latvia
[6]Discovery Biology, Muna Therapeutics, Leuven, Belgium
[7]Department of Human Genetics, KU Leuven, Leuven, Belgium
[8]These authors contributed equally
[9]Lead contact
*Correspondence: mark.fiers@kuleuven.be (M.F.), b.strooper@ukdri.ac.uk (B.D.S.)
https://doi.org/10.1016/j.celrep.2024.114216

SUMMARY

The amyloid plaque niche is a pivotal hallmark of Alzheimer's disease (AD). Here, we employ two high-resolution spatial transcriptomics (ST) platforms, CosMx and Spatial Enhanced Resolution Omics-sequencing (Stereo-seq), to characterize the transcriptomic alterations, cellular compositions, and signaling perturbations in the amyloid plaque niche in an AD mouse model. We discover heterogeneity in the cellular composition of plaque niches, marked by an increase in microglial accumulation. We profile the transcriptomic alterations of glial cells in the vicinity of plaques and conclude that the microglial response to plaques is consistent across different brain regions, while the astrocytic response is more heterogeneous. Meanwhile, as the microglial density of plaque niches increases, astrocytes acquire a more neurotoxic phenotype and play a key role in inducing GABAergic signaling and decreasing glutamatergic signaling in hippocampal neurons. We thus show that the accumulation of microglia around hippocampal plaques disrupts astrocytic signaling, in turn inducing an imbalance in neuronal synaptic signaling.

INTRODUCTION

Alzheimer's disease (AD) is the most common form of dementia, characterized by progressive neurodegeneration that spreads throughout the brain. Widespread deposition of amyloid-β (Aβ) into plaques is a key neuropathological hallmark of the disease. Recent studies in the field have elucidated the importance of studying the cellular phase of this disease.[1] Changes in microglia and astrocytes have been strongly implicated in disease progression, with disease-associated microglia (DAMs)[2–4] and disease-associated astrocytes (DAAs)[5–7] identified as cell states that are strongly associated with AD.

However, studying the interaction of these cells, and how they spatially relate to the neuronal dysfunctions in AD, has long been limited by the available techniques. We previously identified a network of co-expressed genes, termed plaque-induced genes (PIGs), which co-localize with amyloid plaques and whose connectivity and expression levels increase with increasing Aβ load in App^{NL-G-F} mice.[8] The microglial and astrocytic nature of the PIGs provides evidence for a spatially determined multicellular response to amyloid stress, involving the complement system, oxidative stress, and inflammation. The identification of this module suggests that the microglia-astrocyte interaction strengthens with an increasing plaque load.[8] The low resolution of spatial transcriptomics (ST) methodologies at the time hindered our ability to dissect specific cell-type responses. Since then, the rapid advancement in ST has ushered in a number of platforms that boast cellular and subcellular resolution.

In order to study cellular interactions using high-resolution ST, reliable cell segmentation, ideally based on morphology markers rather than simply a nuclear stain, is important to accurately assign transcripts to cells. Here, we decided to take advantage of the CosMx platform, as its large panel of 950 genes provides us with the possibility to not just identify cell types of interest but to also query receptor-ligand (RL) interactions.[9] In parallel, we tested the sequencing-based Spatial Enhanced Resolution Omics-sequencing (Stereo-seq)[10,11] technique, which allows for the unbiased profiling of the transcriptome, albeit with a cell segmentation reliant only on a nuclear stain. Both technologies are commercially available and therefore feasible for institutes

and core facilities to set up with ease, and they have both shown promise in previously published studies, such as in the field of brain regeneration[11] and cancer research.[12]

In this study, we assessed what further insights the CosMx and Stereo-seq technologies can shed on the amyloid plaque niche. We thus explored microglia- and astrocyte-driven glial responses and interactions in our AD model and described the ways in which their signaling pathways are disrupted in the vicinity of plaques.[8] We also describe the heterogeneity of the plaque niche and demonstrate how this heterogeneity—and the glial responses captured within it—can subsequently influence signaling pathways in glial and neuronal cells in the local plaque environment. In performing the relevant analyses, we demonstrate that the cellular resolution provided by CosMx is essential in identifying and exploring signaling pathways. The deeper sequencing depth of the Stereo-seq platform allows us to validate gene expression changes and extend our analyses to biological pathways, but the fact that there is no direct identification of the cell morphology hampers the full realization of this unbiased and highly resolved approach. We discuss some shortcomings that need to be considered when using either technology to study the molecular neuropathology of AD.

RESULTS

For both Stereo-seq and CosMx experiments, we used coronal sections from $App^{NL\text{-}G\text{-}F}$ mice[13] (Figures 1A and 1E). Coronal sections from C57BL/6 wild-type mice were also profiled using Stereo-seq. This matches the brain regions and mouse models used in our previous ST study.[8]

Using the CosMx platform, we analyzed data from four 18-month-old $App^{NL\text{-}G\text{-}F}$ mice, covering the hippocampus and adjacent regions (Figure 1A). The sections were also directly stained for Aβ using the monoclonal Aβ antibody MOAB-2 (Figure 1D). For Stereo-seq, we obtained three adjacent coronal brain cryosections (each 10 μm apart) from one 3-month-old $App^{NL\text{-}G\text{-}F}$ mouse and one age-matched control, as well as from two 18-month-old $App^{NL\text{-}G\text{-}F}$ mice and one age-matched control (Figure 1E). The two outer sections were stained for amyloid pathology using the 6E10 antibody, whereas the middle one was processed for Stereo-seq sequencing. Sequenced transcripts were binned into 20 × 20 DNA nanoballs (DNB)[10] to obtain a total of 2,425,202 pseudo-cells, each with a size of 10 μm in width/height, across the five chips (Figure S1H). We aligned the two adjacent sections from each sample to annotate each pseudo-cell with its respective distance to the nearest edge of plaque pathology.

Cell identification in CosMx and use of pseudo-cells in Stereo-seq

Across the 37,840 high-quality cells in the CosMx dataset, we were able to clearly identify the major expected cell types (Figures 1B and S1A). We note that the glutamatergic neurons clustered into distinct clusters, identified as somatosensory (S1) pyramidal, CA1–CA3, CA4, and dentate gyrus (DG) neurons based on their spatial distribution within the tissue (Figure 1C).

In contrast, in the much larger Stereo-seq dataset, we were not able to recapitulate distinct cell-type clusters or confidently annotate cells with cell types using nuclear-staining-based cell-segmented data[10] (Figures S1F and S1G). Cell segmentation is particularly complex in the brain, in contrast to other tissues, because of the high autofluorescence of the tissue, its complex cell shapes, and a lack of reliable cell membrane markers. We hypothesize that the effect of RNA diffusion,[10] along with the difficulty of segmentation, prevented the generation of "clean" cells that could be confidently annotated. We therefore performed downstream analyses using 20 × 20 DNB binned pseudo-cells as indicated (Figure S1H). To confirm that this binning approach yields biologically relevant information, we scored the Stereo-seq pseudo-cells[10] on their expression of PIG module genes (Figure 1F). Pseudo-cells with high PIG expression superimpose over the plaque staining (Figure 1G), confirming that we can generate biological meaningful data using the Stereo-seq pseudo-cells.

The amyloid plaque niche

We have previously shown the complex global cellular responses that reflect astro- and microgliosis and neuroinflammation in the amyloid plaque cellular niche.[8] The CosMx data revealed that, compared to other cell types, microglia are vastly overrepresented in close proximity to plaques (within 10 μm) (Figure 2A). Using a continuous differential expression, we confirmed that the gene expression of these microglial cells is altered depending on their distance to pathology (Figure 2B). Marker genes for homeostatic microglia (HM), such as *Cx3cr1* and *Tmem119*, are downregulated in microglia in proximity to plaques (Figure 2B, left), while DAM markers,[2,3] including *Apoe*, *Lpl*, and *Trem2*, are upregulated. Interestingly, DAA genes,[5] such as *Gfap*, are also significantly upregulated in astrocytes as they approach plaques (Figure 2C, left).

This shift in cell states in function of distance to pathology was corroborated in the Stereo-seq dataset; by correlating the mean PIG expression levels of pseudo-cells with their distance to plaques, we confirmed the higher expression of PIG module genes near plaque pathology ($r_s = -0.855$, $p = 2.22e{-}58$) at 18 months (Figure 2E). Meanwhile, this correlation was much weaker at 3 months ($r_s = -0.122$, $p = 0.034$) (Figure S1E), supporting our previous finding that the PIG response is an age-dependent response that develops over time.[8]

To investigate whether microglia and astrocytes display similar responses to plaques across different brain regions, we compared the responses of these cells to plaques in either the hippocampus or the cortex. We found that microglial genes showed a similar differential expression profile as the cells approached plaques, regardless of brain region (Figure 2B, right). In astrocytes, in contrast, we observed a broader spread in responses, suggesting a region-specific aspect of the astrocytic response to plaque pathology (Figure 2C, right). To validate this, we turned to Stereo-seq and found that microglial DAM genes are consistently and similarly upregulated in pseudo-cells in the proximity of plaques, independent of whether they are located in the isocortex or hippocampus (Figure 2F, $r_s = 0.817$, $p < 2.2e{-}16$). The astrocytic DAA genes show greater regional variability (Figure 2G, $r_s = 0.583$, $p < 2.2e{-}16$). A Fisher's z-test for differences of correlations indicates that the two correlations are indeed significantly different ($p = 8e{-}6$). Astrocytic DAA

CellPress
OPEN ACCESS

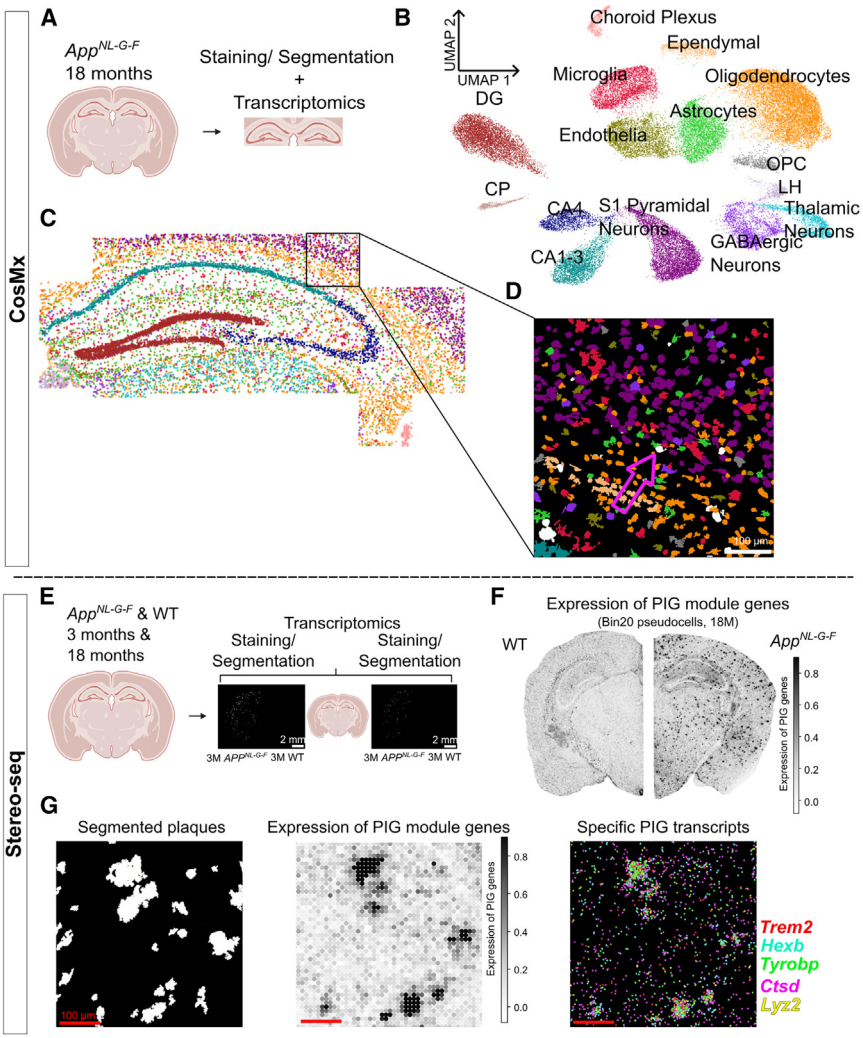

Figure 1. Resolving the plaque niche using spatial transcriptomics

(A) Experimental setup for the CosMx experiments. The hippocampus and adjacent cortical regions of one coronal section from four 18-month-old *App*$^{NL\text{-}G\text{-}F}$ mice were assessed. Plaques were resolved in the same section using the monoclonal Aβ antibody MOAB-2.

(B) Uniform manifold approximation and projection (UMAP) showing the 37,840 segmented CosMx cells. Cells were unbiasedly clustered using the Leiden algorithm and annotated using a reference mouse brain dataset.[14] The glutamatergic neurons were further resolved into subclusters, which were annotated according to spatial location.

(C) Spatial localization of the cells of an individual tissue section, colored by Leiden cluster (as shown in B). Spatially resolving the clusters facilitated the annotation of the glutamatergic neuron subtypes.

(D) Zoom-in image of segmented plaques (white) overlaid with segmented cells (colored by Leiden cluster, as shown in B and C) in the same coordinate space. One representative plaque is highlighted with the arrow.

(E) Schematic of the experimental setup for the Stereo-seq experiment. Two full coronal sections of 18-month-old *APP*$^{NL\text{-}G\text{-}F}$ mice and one full coronal section from an age-matched control were analyzed. For the 3-month time point, two-half coronal sections were analyzed for the *APP*$^{NL\text{-}G\text{-}F}$ mice and two-half coronal sections for the age-matched controls. Amyloid pathology was stained with the 6E10 antibody on adjacent slides and aligned with the transcriptome using the Fiji "Landmark correspondences" macro.

(F) Pseudo-cells from an 18-month-old AD and an age-matched control hemisphere scored and colored based on relative expression of the PIG module (white: low expression of PIG, black: high expression). Pseudo-cells in the AD hemisphere show marked elevation of PIG expression. Scores were obtained using the *score_genes()* function in SCANPY.

(G) Left: representative image of segmented plaques in white from an 18-month-old *App*$^{NL\text{-}G\text{-}F}$ mouse. Middle: pseudo-cells in the same coordinate space as above scored on expression of the PIG module (black: high expression of PIG). Right: spatial location of select PIG module transcripts (*Trem2*, *Hexb*, *Tyrobp*, *Ctsd*, *Lyz2*), also in the same coordinate space. Scale bar represents 100 μm except for (E), where the scale bar represents 2 mm. CP, caudate putamen; OPC, oligodendrocyte progenitor cell; LH, lateral habenula. For CosMx, 4 biological replicates were used, and for Stereo-seq 5 were used.

genes that show increased expression in the hippocampus close to plaques in comparison to the cortex included *Itm2b*, *Cpe*, and *C1qa*. On the other hand, the astrocytic cortical response to plaques was characterized by *Atp1a1*, *Ckb*, and *Kcnip4*. Based on these findings, we propose region-specific differences in astrocytes and their response to plaques. Previous work has shown that astrocytes display region-specific differences in expression levels,[15] and as such, it is not surprising that they also display region-specific responses to plaques. With this in mind, we will focus subsequent analyses relating to astrocytes specifically within the hippocampus.

Given the dual microglial-astrocytic nature of the PIG genes, we wondered to what extent we could find evidence for a disruption in the direct crosstalk between, and within, these glial cell types in proximity to plaque pathology. We thus sought to identify candidate disrupted PIG RL pairs between microglia and astrocytes.

For this, we used the CellPhoneDB algorithm[16] to predict which RL pairs were likely to be active between cell types, with a specific focus on pairs where at least one component was significantly differentially expressed with respect to distance to pathology. Based on a public database of annotated RL pairs, the algorithm investigates which RL pairs are cell-type specific and assigns a strength to the candidate pairs based on the expression of the receptor and the ligand.[16] For the predicted RL pairs from CellPhoneDB, we took advantage of the spatial information afforded by the CosMx dataset and tested (1) whether RL pairs do indeed co-occur in the same neighborhood and, if so, (2) how the "strength" of the co-occurrence of the components changes in different environments (e.g., as cells approach

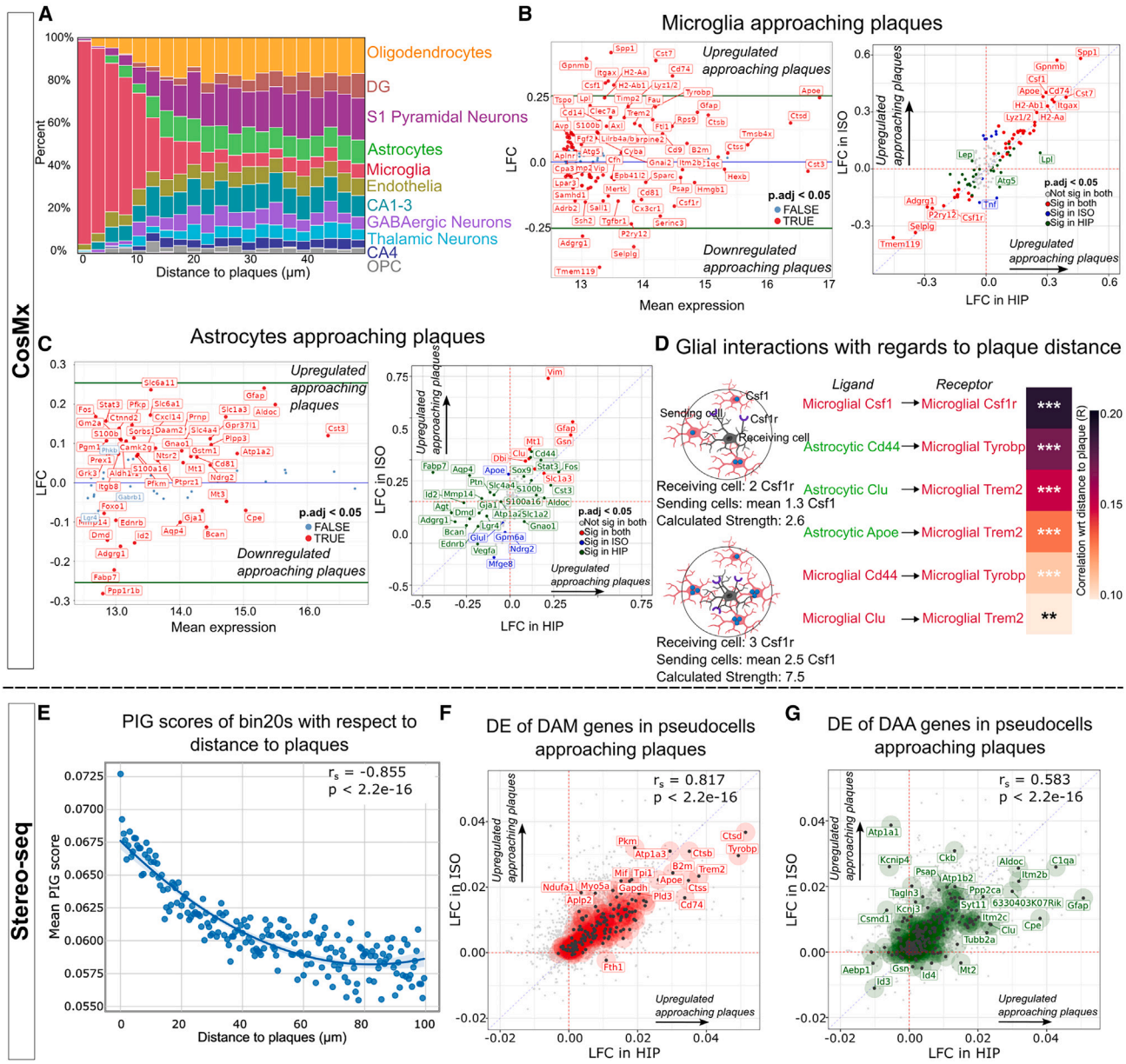

Figure 2. Cellular responses to plaques

(A) Histogram showing the relative cell-type composition of cells at varying distances to plaques, as resolved in the CosMx dataset of tissue sections from $n = 4$ App^{NL-G-F} mice.

(B) Left: MA plot showing gene differential expression in microglial cells with respect to distance to plaques (as a continuous covariate), with the x axis showing mean expression and the y axis log fold change (LFC). Genes above the blue line (y = 0) represent genes that show an increased expression in the analyzed cells, as these cells get closer to pathology. The top green line indicates an LFC that represents a doubling in the gene expression (i.e., FC = 2) for every 50 μm that the cell gets closer to a plaque, while the bottom green line indicates an LFC that represents a halving of the gene expression for every 50 μm. An empirical Bayes quasi-likelihood F-test (QLFTest) was used, and *p* values were adjusted with Benjamini-Hochberg correction (*p*.adj <0.05). Significantly changed genes are labeled in red. Right: quadrant plot comparing the transcriptomic responses of microglia to plaque pathology in the isocortex (y axis) and in the hippocampus (x axis) in the CosMx dataset. Red: genes significant in both comparisons; gray: genes not significant in either comparison; blue: genes significant in isocortical microglia only; and green: genes significant in hippocampal microglia only. An empirical Bayes QLFTest was used, and *p* values were adjusted with Benjamini-Hochberg correction (*p*.adj < 0.05).

(C) Left: the MA plot showing gene differential expression in astrocytes with respect to distance to plaques (as a continuous covariate), with the x axis showing mean expression and the y axis LFC. Genes upregulated in cells approaching are shown above the blue line (y = 0). The top green line indicates an LFC that represents a doubling of the gene expression (i.e., FC = 2) for every 50 μm that the cell gets closer to a plaque, while the bottom green line represents an LFC that represents a halving of the gene expression for every 50 μm. An empirical Bayes QLFTest was used, and *p* values were adjusted with Benjamini-Hochberg correction (*p*.adj < 0.05). Significantly changed genes are labeled in red. Right: the quadrant plot comparing the transcriptomic responses of astrocytes to

(legend continued on next page)

plaques). We therefore calculated RL strengths on an individual cell level for each receiving cell by taking into account the expression level of the receptor in the receiving cell and the average expression of the ligands from sending cells in a 50 μm radius of the receiving cell (see schematic in Figure 2D, left).

We applied this approach to the predicted RL pairs between microglia and astrocytes in which either the receptor or the ligand was previously identified as a PIG.[8] Across our whole dataset, CellPhoneDB identified 130 candidate RL pairs between microglia and astrocytes, of which 11 are PIGs. We found that the strength of the identified PIG RL pairs significantly increased in strength as the cells approached plaques (Figure 2D, right). As microglia approached plaques, the strength of microglia-to-microglia signaling such as the Csf1 → Csf1r interaction and the Cd44 → Tyrobp interaction became stronger. Both *Cd44* and *Tyrobp* are markers for DAM.[3] The astrocyte-to-microglia crosstalk takes the form of astrocytic Cd44, Clu, and Apoe interacting with microglial Tyrobp and Trem2 (Figure 2D), with *Clu* and *Apoe* being markers for DAA.[5] *CD44* has also been shown to be associated with a DAA-like state in samples from patients with AD.[17] This suggests that as cells approach plaques, the development of DAMs could be in part driven by the astrocytic signals the microglia receive and that the PIG network does indeed encapsulate signaling pathways between microglia and astrocytes. As we were limited by the genes in the CosMx panel, there are likely other RL pairs that form part of the PIG network that we could not interrogate.

Cellular effects within the plaque niche

We next explored the cellular variations in the different cellular niches, defining the plaque niche as all cells located within 40 μm of a plaque edge. By counting the number of cells within this area, we find that the cellular composition of niches is highly heterogeneous, with the average CosMx plaque niche (represented in Figure 3A) containing 3 microglia (but they can contain as many as 11 microglia, shown in Figure S2B), 1 astrocyte (maximum [max] 5 astrocytes), 1 oligodendrocyte (max 12 oligodendrocytes), 1 GABAergic (max 12 GABAergic neurons), and 2 glutamatergic neurons (max 24 glutamatergic neurons). As the amyloid plaque varies in size, different plaque niches contain varying total cell counts. To account for this, we compared the cell-type densities (calculated as the numbers of each cell type divided by the total number of cells present in a specific plaque niche) across plaque niches. A uniform manifold approximation and projection (UMAP) reflective of the cell-type compositions of plaque niches reveals a notable heterogeneity with respect to relative microglial densities, as well as the other cell types (Figures 3B and S2A).

To validate this heterogeneity using Stereo-seq, we first pseudo-bulked all the transcripts that fall within a plaque niche (defined here as the area within 40 μm of the plaque edge, see Figure 3A). Unbiased clustering of the transcriptomes of these plaque niches (Figure 3F) suggested that the transcriptomic heterogeneity in plaque niches is strongly driven by region. Next, we deconvolved each of the pseudo-bulked plaque niche transcriptomes into different cell types using the cell2location algorithm[18] and a well-established mouse brain reference dataset[14] (Figures 3G and S2E). In this way, we obtained the predicted number of each cell type that composes each microenvironment. By plotting the predicted number of neuronal subtypes on the transcriptomic UMAP, we confirmed that the presence of region-specific neurons drives the overall transcriptomes of the plaque niches (Figure S2D). Using the estimations obtained from cell2location, we again found that plaques are heterogeneous in their cell-type compositions (Figures 2G and S2E). Notably, microglial densities in plaque niches range from 4% to 50% (Figure 3G), corresponding to a range of 0.3–20 estimated microglial cells per plaque niche (Figure S2F). This heterogeneity in microglial densities can be observed in all analyzed brain regions (Figure 3G) and is particularly pronounced in plaques from 18-month-old mice (Figure 3H), suggesting that as amyloid plaque niches mature over time, the number of microglia around them increases.

We assessed how the transcriptomes of microglia and astrocytes change depending on the composition of the plaque niche they belong to. In CosMx, we scored each microglia on its expression of DAM genes and found a positive correlation between the microglial density of a plaque niche and the microglial DAM score of said plaque niche (Figure 3C). We performed a differential expression of all astrocytes sitting in a plaque niche with respect to their respective plaque niche's microglial density

plaque pathology in the isocortex (y axis) and in the hippocampus (x axis). A stronger response of astrocytes is seen in the isocortex. Red: genes significant in both comparisons; gray: genes not significant in either comparison; blue: genes significant in cortical astrocytes only; and green: genes significant in hippocampal astrocytes only. An empirical Bayes QLFTest was used, and p values were adjusted with Benjamini-Hochberg correction ($p.adj < 0.05$).

(D) From the predicted receptor-ligand (RL) pairs between microglia and astrocytes (obtained from CellPhoneDB), all pairs containing PIG module genes were extracted. Left: a schematic showing how the co-occurrence of RL was calculated using the example of the Csf1-Csf1r RL pair between microglia and microglia. The expression of the receptor (Csf1r, drawn in purple) on the receiving cell (shown in black) was multiplied with the average expression of the ligand (Csf1, drawn in blue) expressed in neighboring sending cells (red), defined as sitting within a 50 μm radius of the receiving cell. Right: the changes in RL strength of specific pairs were calculated as the receiving cells expressing the receptor were approaching plaques. The Pearson correlation coefficient (R) was plotted. All plotted RL pairs had a positive correlation, indicating increased RL strength as the cells were approaching plaques.

(E) Mean PIG expression levels of 18-month-old Stereo-seq pseudo-cells (y axis) at a given distance from plaques (x axis), within 100 μm of a plaque edge. The solid line represents the fit of a second-order polynomial equation, with the 95% confidence interval shown by the translucent bands. The PIG score increases as pseudo-cells approach plaques. The Spearman correlation coefficient (r_s) and its respective p value were calculated.

(F) Quadrant plot showing the LFCs of genes in pseudo-cells with respect to distance to pathology in the hippocampus (x axis) and isocortex (y axis). Red: DAM marker genes. LFCs were calculated using an empirical Bayes QLFTest. r_s values were calculated using Spearman's correlation.

(G) Quadrant plot showing the LFCs of genes in pseudo-cells with respect to distance to pathology in the hippocampus (x axis) and isocortex (y axis). Green: DAA marker genes. LFCs were calculated using an empirical Bayes QLFTest. r_s values were calculated using Spearman's correlation. ISO, isocortex; HIP, hippocampus. $^{**}p < 0.01$ and $^{***}p < 0.001$.

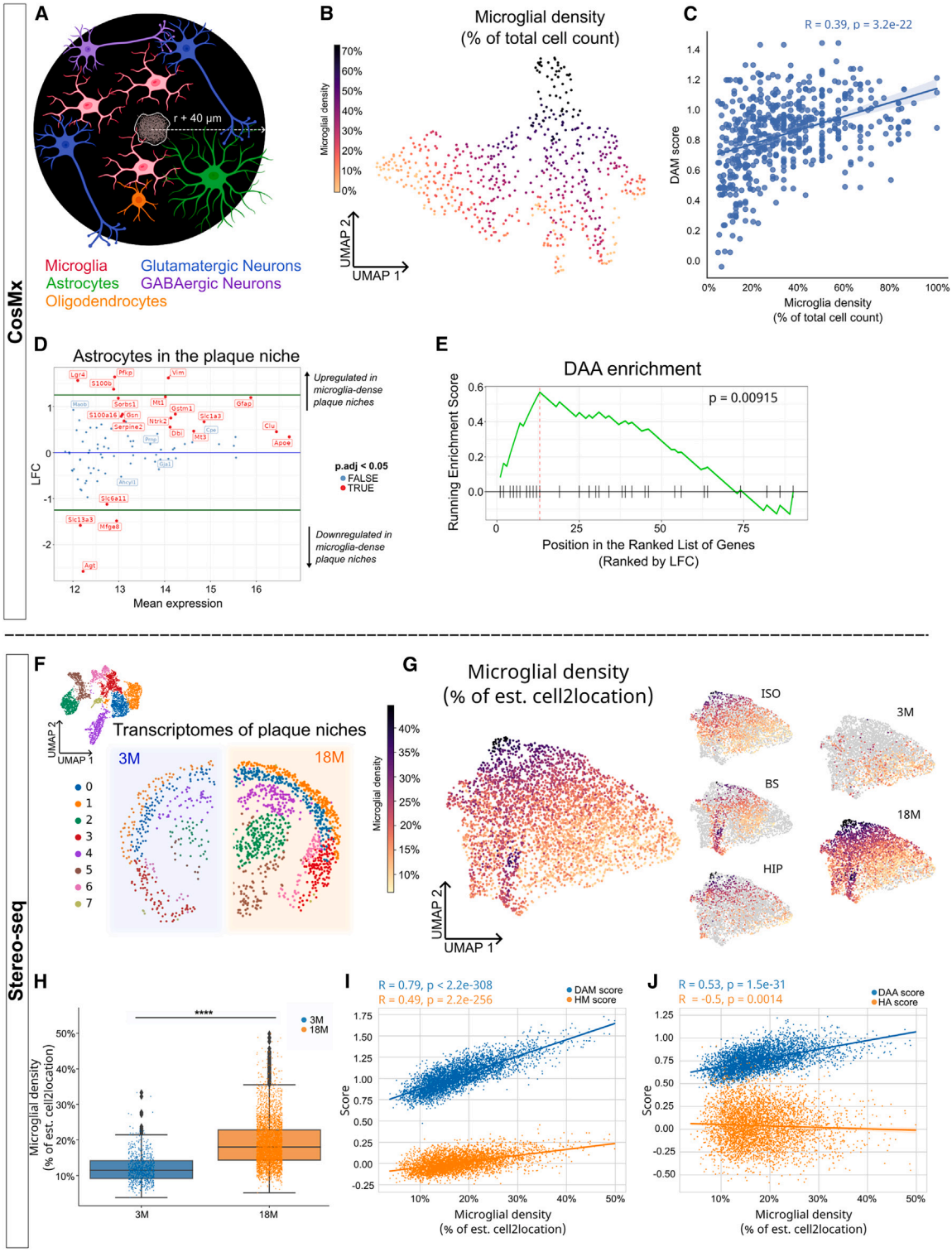

Figure 3. Heterogeneity of the cellular composition of the amyloid plaque niche

(A) A representative diagram highlighting the average cellular composition of a plaque niche. The plaque niche is defined as a circle with a center equal to the plaque niche's centroid and a radius (r) equal to the plaque niche's radius +40 µm. The average amyloid plaque cellular niche is composed of three microglia (red), one oligodendrocyte (orange), one astrocyte (green), one GABAergic neuron (purple), and two glutamatergic neurons (blue). The sizes of the different cell types are not to scale. Please note that the cellular composition of the amyloid plaque niche varies strongly as discussed in the text and below.

(legend continued on next page)

(Figure 3D) and likewise saw an upregulation of canonical DAA markers, such as *S100b* and *Pfkp*,[19] and a downregulation of homeostatic astrocyte (HA) genes, such as *Mfge8*.[5] *Mfge8* has previously been shown to be able to reverse the neurotoxic DAA-like phenotype in astrocytes.[20] To confirm this trend, we performed a gene set enrichment analysis (GSEA), in which we tested for the enrichment of DAA (i.e., activated neurotoxic astrocytic) marker genes in the differential expression. The GSEA revealed a significant enrichment of DAAs in highly microglia-dense plaque niches (Figure 3E). In addition to changes in the astrocytic cell state, we also observed changes in neurotransmitter transporters, such as a decrease in *Slc6a11* expression in astrocytes, as they sit in microglia-dense plaque niches (Figure 3D). The presence of extracellular GABA is tightly regulated, and *Slc6a11* encodes for the astrocytic GABA transporter Gat3, which can take up GABA from the extracellular space.

We also saw the shift in microglial and astrocytic cell states in Stereo-seq, where we assessed the relationship between the predicted number of microglia in a plaque niche and the relevant expression of either DAM or HM genes in the niche (Figure 3I). We saw that plaque niches with more microglia had a higher HM score, which is to be expected since more microglia in the plaque niche inevitably means that there will be more microglial transcripts—even homeostatic ones—present in the plaque niche. However, the fact that the DAM score increases at a faster rate than the HM score indicates that these microglia increasingly upregulate DAM genes as they inhabit more microglia-dense niches. Similarly, we saw an increase in DAA genes, while the marker genes for HA showed a small decrease (Figure 3J). This supports the hypothesis based on the CosMx data that more microglia-dense plaque niches could represent a more severe local plaque environment, characterized by the concurrent development of DAMs and DAAs.

Neuronal responses to the glial changes in the amyloid plaque niche

We next investigated whether these changes in plaque severity corresponded to an effect on other cells in the plaque niche. Interestingly, in the CosMx dataset, we see that astrocytes participate in the highest number of RL pairs as the sending cell (Figures 4A and S3A). Astrocytes have around 15–20 RL pairs with other cells, which is around three to four times more than other sending cells (0–5 RL pairs shared with other cell types) (Figure S3A). Even when normalizing the number of RL pairs to the number of genes analyzed for each cell type, we still see a dramatic increase in the number of RL pairs in astrocytes (Figure 4A). This was especially striking given that only 28 of our analyzed astrocytic genes in CosMx are found in the CellPhoneDB database, in contrast to 66 microglial and 57 genes from CA1–CA3, for example. All this combined indicates the importance of astrocytic signaling in the intercellular interactions once the cells are exposed to a local plaque environment.

Considering the differential expression of the GABA transporter *Slc6a11* observed in the astrocytes in microglia-dense plaque niches (Figure 3D), we investigated the signaling pathways postulated between astrocytes and the neurons within the hippocampus. For this, we calculated the strength of co-occurring RL pairs (as discussed above and shown in Figure 2D) between astrocytes (as the sending cells) and the neuronal cell types (as the receiving cells). We found that GABA-signaling

(B) A UMAP of the $n = 619$ CosMx plaque niches (across hippocampal sections from $n = 4$ 18-month-old App^{NL-G-F} mice) was generated based on the cell-type densities in the neighborhood of each plaque. Each point represents a plaque niche, colored by its estimated microglial density, expressed as the percentage of the total cell count in the niche. Only plaque niches with at least 5 cells were included in the analysis.
(C) Pearson correlation (and its associated p value) between the microglia density in plaque niches (x axis) and the highest microglial DAM score in said plaque niche (y axis).
(D) MA plot showing differentially expressed genes in astrocytes sitting in a plaque niche with respect to the microglia density of said plaque niche (as a continuous covariate), with the x axis showing mean expression and the y axis LFC. Significantly changed genes are labeled in red. The top green line indicates an LFC that represents a doubling of the gene expression (i.e., FC = 2) as microglial density in the plaque niche increases from 0% to 75%, while the bottom green line indicates an LFC that represents a halving of the gene expression for the same increase in microglial density. An empirical Bayes QLFTest was used, and p values were adjusted with Benjamini-Hochberg correction (p.adj < 0.05).
(E) From the differential gene expression analysis in (D), we performed gene set enrichment analysis (GSEA) to further explore shifts in the astrocytic phenotype. We saw a significant positive enrichment of DAA genes in astrocytes that sit in microglia-dense plaque niches, indicating that astrocytes adopt a more DAA-like phenotype in these plaque niches. The thick black line indicates the running enrichment score across the FC-ranked genes (x axis), while the vertical dotted red line indicates where the enrichment score peaks. Black vertical tick marks along the x axis show the location of individual DAA genes within the FC-ranked gene list. The p value was calculated by permutation analysis.
(F) UMAP representing the integrated and unbiasedly clustered transcriptomes of $n = 4{,}285$ Stereo-seq plaque niches from all 18- and 3-month-old App^{NL-G-F} mice and the spatial distribution of the clusters in a 3- and an 18-month-hold hemisphere. Plaque niches are unbiasedly clustered using the Leiden algorithm.
(G) Left: the UMAP of the Stereo-seq plaque niches generated based on estimated cell-type densities, calculated using cell2location. Each point in the UMAP represents a plaque niche, colored by its estimated microglial density (calculated by dividing the number of estimated microglia by the total number of estimated cells in the plaque niche). Cell-type densities were estimated using cell2location. Right: the same UMAP but with only plaque niches belonging to a certain region or to a certain age colored according to estimated microglial density. The remainder of the plaque niches are shown in gray.
(H) Boxplots comparing predicted microglial densities in the plaque niches of 3-month-old ($n = 682$ niches) to those of the 18-month-old mice ($n = 3{,}603$ niches). The boxes represent the quartiles of the datasets (with the middle line indicating the median), while the whiskers extend to the lower and upper limits of the distribution, with the exception of outlier points. Mann-Whitney U test. Microglial densities are predicted with cell2location.
(I) Blue: correlation of estimated microglial densities (x axis) in each Stereo-seq plaque niche and the expression level of DAM marker genes in the plaque niche (DAM score, y axis). Orange: correlation of estimated microglial densities (x axis) and the expression level of HM marker genes (HM score, y axis). Pearson correlation. Microglial densities were estimated using cell2location.
(J) Blue: correlation of estimated microglial densities (x axis) in each Stereo-seq plaque niche and the expression of DAA marker genes in the plaque niche (DAA score, y axis). Orange: correlation of estimated microglial densities (x axis) and the expression of HA marker genes (HA score, y axis). Pearson correlation. Microglial densities were estimated using cell2location. ISO, isocortex; BS, brainstem; HIP, hippocampus; 3M, 3 months; 18M, 18 months. ***$p < 0.001$.

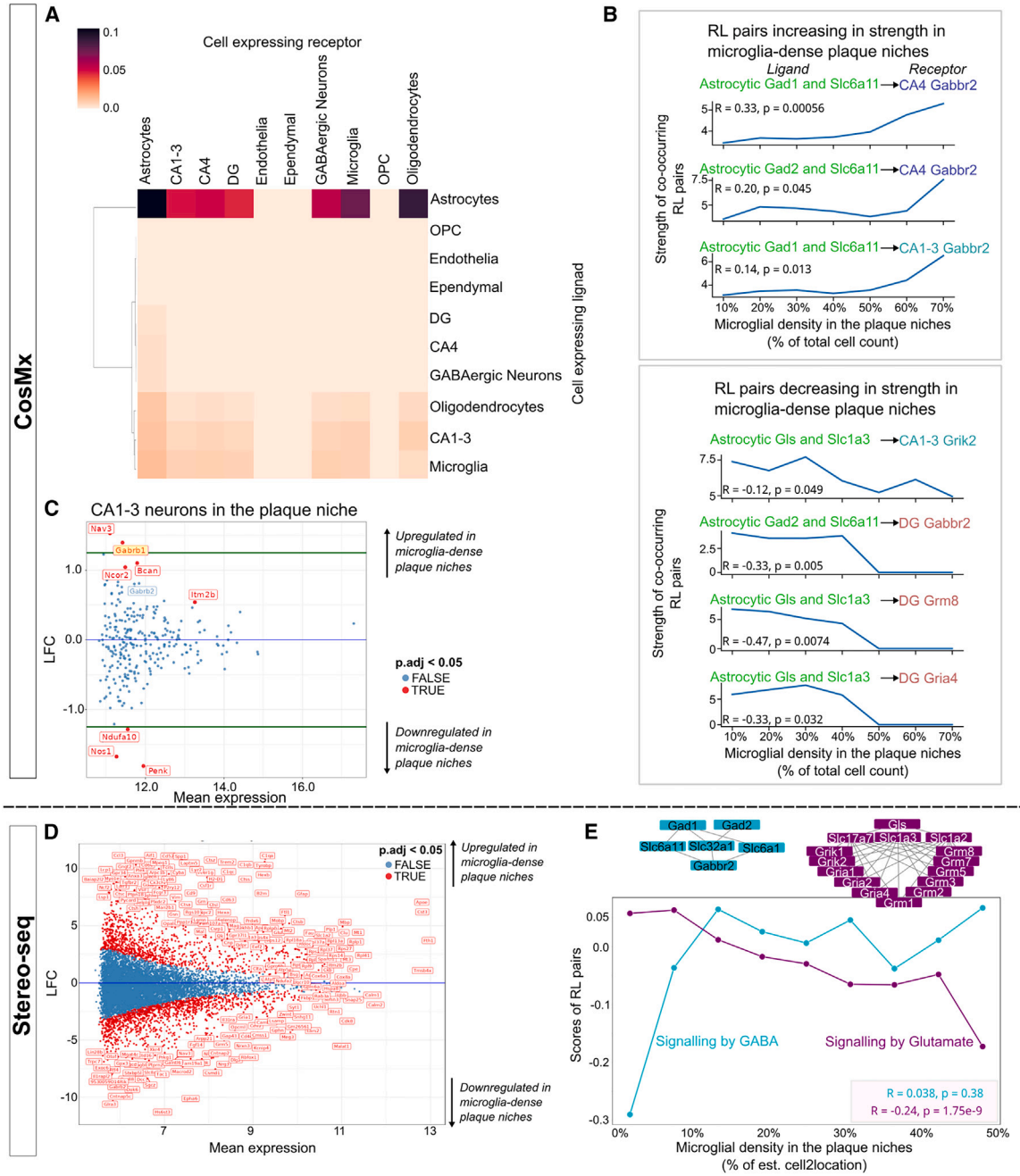

Figure 4. Cellular interactions in the plaque niche

(A) Number of RL pairs between different cells in the $n = 316$ CosMx hippocampal plaque niches as predicted by CellPhoneDB. The number of predicted RL pairs between a receiving cell type expressing the receptor and a sending cell type expressing the ligand was divided by the number of genes analyzed for both cell types in CosMx. Astrocytes show a high number of RL interaction pairs with other cell types.

(B) Strength of the RL pairs between astrocytes and neurons in the hippocampus that show a significant correlation with microglial density of the plaque niche. Pearson correlation (and its associated p value) were plotted.

(C) MA plot showing gene differential expression in CA1–CA3 neurons in a plaque niche with respect to microglial density in said plaque niche (as a continuous covariate), with the x axis showing mean expression and the y axis LFC. Significantly changed genes are labeled in red, while the gene associated with GABA signaling, *Gabrb1*, is highlighted in yellow. The top green line indicates an LFC that represents a doubling of the gene expression (i.e., FC = 2) as microglial density in the plaque niche increases from 0% to 75%, while the bottom green line indicates an LFC that represents a halving of the gene expression for the increase in microglial density. An empirical Bayes QLFTest was used, and p values were adjusted with Benjamini-Hochberg correction (p.adj < 0.05).

(D) MA plot showing gene differential expression in $n = 641$ 18-month-old hippocampal Stereo-seq plaque niches (pseudo-bulked) with respect to the niche predicted microglial density, as predicted by cell2location (as a continuous covariate). Genes upregulated with higher microglial density are shown above the

(legend continued on next page)

RL pairs between astrocytes and CA1–CA3 and CA4 neurons (astrocytic *Gad1/2* + *Slc6a11* to neuronal *Gabbr2*) increase in strength (Figure 4B, top) as the plaque niches these neurons inhabit become more densely packed with microglia. In line with this, we found *Gabrb1*, a subunit of the GABAergic type-A receptor, upregulated in CA1–CA3 neurons in microglia-dense plaque niches, whereas *Gabrb2*, a subunit of the GABAergic type-B receptor, trended toward significance (adjusted *p* value = 0.078) (Figure 4C).

In concordance with these findings, we also saw a decrease in the strength of RL pairs linked to glutamate signaling (astrocytic *Gls* + *Slc1a3* to neuronal *Grik2*, *Grm8*, and *Gria4*) in CA1–CA3 and DG neurons (Figure 4B, bottom). Interestingly, we noted a decrease in a RL pair linked to GABA signaling in the DG neurons (astrocytic *Gad2* + *Slc6a11* to *Gabbr2* on DG), indicating a more complicated relationship between astrocytes and DG cells. In the differential gene expression of CA1–CA3 neurons with respect to plaque niche microglial density, we observed an upregulation of *Nav3*, which regulates axon guidance and has been shown to be upregulated in patients with AD.[21,22] Neurons expressing the protein have been demonstrated to show strong degenerative morphology.[22] On the other hand, *Nos1*, encoding neuronal nitric oxide synthase (nNOS), decreases in CA1–CA3 neurons (Figure 4C). nNOS in hippocampal neurons has been linked to long-term potentiation[23] and can act to increase glutamatergic neurotransmission.[24]

To further confirm the disruption in synaptic signaling identified in CosMx, we used the Stereo-seq dataset to investigate changes in the transcriptome of hippocampal plaque niches as the estimated microglial density increased (Figure 4D). We saw a downregulation of terms associated with synaptic function (like "neurotransmitter secretion" and "synapse assembly") in microglia-dense plaque niches (Figure S3B). In lieu of reliable cell segmentation, we scored the pseudo-bulked plaque niches on their expression of the predicted RL pairs from the CosMx CellPhoneDB analysis, doing so separately for pairs associated with GABA signaling and with glutamate signaling. We found that the pairs linked to glutamate signaling decreased as microglial density increased (Figure 4E), whereas we saw no statistically significant changes in pairs linked to GABA signaling. Taken together, these findings confirmed that astrocytic signaling around plaque pathology is disrupted with increasing microglial density, which in turn induces an imbalance in synaptic signaling in neurons in the hippocampus.

DISCUSSION

In this study, we employed two novel high-resolution ST techniques to study the local cellular and gene expression changes around Aβ plaques in a mouse model of AD. We assessed the regional specificity of microglial and astrocytic responses to plaques and confirmed that components of the previously identified PIG network represent microglial-astrocytic crosstalk. Furthermore, we found heterogeneity in the cellular composition around plaques, with the DAM and DAA phenotypes specifically developing around microglia-dense plaques. Notably, we identified astrocytes as a key hub of cellular interactions in the plaque niche that impairs neuronal synaptic functioning, increasing GABAergic signaling and decreasing glutamatergic signaling.

It is well known that the transcriptomes of glial cells are altered in AD pathology, as characterized previously by the DAM and DAA phenotypes, and that these develop as the cells approach plaques.[25] It appears that the microglial response in the plaque niche is a generic response that is consistent across brain regions (Figures 2B, right, and 2F), confirming previous work that DAMs develop independent of the hippocampus or cortex region.[3] On the other hand, astrocytes display a heterogeneous response to plaques dependent on their brain region of origin (Figures 2C, right, and 2G). Other studies have shown that astrocytes display region-specific differences, both in terms of their phenotype[19] and their functions, including calcium signaling.[15] Furthermore, it is also known that hippocampal astrocytes develop more pronounced changes to aging, akin to developing a DAA phenotype, compared to cortical astrocytes.[26] As the DAA signature was originally characterized in hippocampal astrocytes,[5] it seems that astrocytes in other regions of the brain respond differently to plaques. Indeed, since the initial description of the DAA phenotype,[5] work from others has expanded the nomenclature of astrocyte substates.[19,27]

Beyond the cell-type-specific DAM and DAA responses, we have previously found evidence that a microglial-astrocytic PIG response to plaque pathology represents crucial crosstalk between, and within, these two cell types in the plaque niche.[8,25,28] Here, using the single-cell resolution of the CosMx platform, we were able to, in much more detail, probe candidate RL pairs that belong to the PIG network. The RL pair most affected by proximity to pathology was the microglial-microglial Csf1 (ligand) → Csf1r (receptor) pair. Taken together with Csf1r's known role in microglial proliferation,[28] as well as the upregulation of Csf1 in microglia as they approach plaques (Figure 2B), this provides evidence that microglia proliferate and activate one another via Csf1 → Csf1r signaling in the vicinity of plaques. Interestingly, it has previously been documented that plaque-associated microglia, specifically, remain insensitive to elimination by Csf1r inhibitors.[29] The increase we document in Csf1r signaling around plaques (Figure 2D) could potentially make these plaque-associated microglia more resistant to this method of inhibition. We also cannot exclude the possibility that other signaling pathways activated in microglia around plaques confer a protection against Csf1r inhibitors.

We found that a number of the disrupted PIG RL pairs represent astrocyte-to-microglia signaling. The astrocytic signals

blue line (y = 0). Significantly changed genes are labeled in red. A QLFTest was used, and *p* values were adjusted with Benjamini-Hochberg correction (*p*.adj < 0.05).

(E) Based on the predicted RL pairs from the CosMx dataset, we analyzed the expression of genes linked to glutamate (purple) and GABA (blue) signaling. The genes are shown as networks above. Each Stereo-seq plaque niche was scored on its expression of these sets of genes, and the median score of the plaque niches (y axis) at given ranges of microglial density (x axis) was plotted. There is a significant decrease in the glutamate signaling pairs with increasing microglial density in the plaque niche. Pearson correlation.

Cd44, *Clu*, and *Apoe* target the *Trem2* signaling pathway in microglia, by binding to both Trem2 and to its downstream signaling partner Dap12 (Figure 2D), which is a known driver of DAM development.[28] In line with this, in a mouse model where *Apoe* is specifically knocked out in astrocytes, microglia show a downregulation of DAM markers.[30] It should be noted that although our analysis did not identify disruptions in the microglia-to-astrocyte PIG signaling pairs that are present in both the CosMx panel and CellPhoneDB databases, it does not outright exclude the existence of any PIG microglia-to-astrocyte signaling. Instead, this raises the interesting possibility that the communication between microglia and astrocytes in the vicinity of plaques may be a two-way street. In other words, the activation of DAMs as microglia approach plaques could be driven not only by the plaque itself or by autocrine microglia signaling but also by the signals microglia receive from neighboring astrocytes.

We found that as niches increase in their respective microglial densities, a process that appears to happen with time (Figure 3H), the microglia and astrocytes within the niches acquire more disease-associated phenotypes (Figures 3C, 3E, 3I, and 3J), suggesting that microglial density can be used as a proxy for plaque severity; however, this was not correlated with the size of the plaques themselves (Figure S2C). To explore this possibility, we investigated the effect of this plaque severity on other cells in the plaque niche. Interestingly, it turns out that particularly astrocytic, not microglial, signaling to other cells is disrupted as microglia density changes in the plaque niches (Figure 4A). This aligns with previous findings that activated astrocytes can be neurotoxic and suggests that astrocytes play a crucial role in the cellular phase of AD.[6]

We investigated RL pairs between astrocytes and the neurons in the hippocampus due to the fact that we saw a decrease of *Slc6a11*, which encodes the GABA transporter Gat3, in astrocytes in microglia-dense plaque niches (Figure 3D). Blocking Gat3, and therefore GABA uptake, when hippocampal neurons are active has been shown to lead to a hyperpolarization of these neurons due to increased GABA availability.[31] The downregulation of astrocytic *Slc6a11* in high-microglia plaque niches may therefore impair neuronal activity. In line with this, we saw that the strength of co-occurring RL pairs between astrocytes (expressing Gad1/Gad2 and Slc6a11) and neurons, expressing Gabbr2, increased (Figure 4B) within microglia-dense plaque niches. Astrocytes produce GABA through many mechanisms including Gad1 and Gad2,[32] and previous work has shown that GABA release from astrocytes is increased in a model of AD.[33] When GABA release is blocked, these impairments are ameliorated.[34] CA1–CA3 neurons express a range of GABA receptors, which play an important role in synaptic plasticity and memory formation.[35] The level of $GABA_A$ receptors has been found to increase in the CA1 regions in patients with AD.[36]

We also saw putative downregulation of signaling through glutamate (Figures 4B and 4E), mediated through astrocytic *Gls* and *Slc1a3* and neuronal *Grik2*, *Grm8*, and *Gria4*. *Slc1a3* encodes a glutamate transporter to enable clearing of extracellular glutamate. Downregulation of *Slc1a3* was previously found in patients with AD and in AD models, particularly around plaques,[37] and knockout of the gene exacerbated memory deficits in an animal model of AD.[38] *Gria4* is a postsynaptic receptor that plays an important role in excitatory synaptic transmission and whose downregulation on both the transcriptomic and proteomic levels has been shown in patients with AD.[37,39] Furthermore, in Stereo-seq, where we had more statistical power and a wider selection of genes, we found that other neuronal functions, such as "regulation of membrane potential," were disrupted in plaque niches with more microglia (Figure S3B).

Previous studies have shown that neuronal hyperexcitability is an early symptom in AD and related mouse models,[40–42] with a recent study exploring the specific hyperexcitability in a specific subset of neurons in layers 2–3 in the cortex of human patients.[40] In contrast to this, here we propose a loss of synaptic function in the hippocampus driven by astrocytic signals. As we analyzed the mice at a late stage of the disease, we could be missing the preceding hyperexcitability described in the other publications,[42] or there could be region-specific effects between the cortex previously analyzed[40] and the hippocampus, which is particularly likely, as we have shown a heterogeneous response of astrocytes to plaques in these two brain regions (Figure 2C).

Limitations of the study

Overall, while both novel spatial techniques are useful and can be upscaled, further development of data analysis resources and improvements are needed to maximize the output of these approaches. New tools analyzing downstream signaling, such as NicheNet,[43] and RL-independent methods inferring changes in transcriptome in proximity to other cells, such as NCEM,[44] could be used to further explore cell-cell interactions. Reliable cell segmentation remains a limitation in the field overall, however, and as we have demonstrated, this is an important prerequisite to deciphering changes in cellular transcriptomes, disrupted RL pairs, and cellular crosstalk in the cellular phase of AD.

We found that the ability to analyze the CosMx dataset on a single-cell level was vital in driving conclusions about the amyloid plaque niches, including glial responses and crosstalk, as well as the downstream neuronal responses, within them.

While the Stereo-seq dataset proved to be complementary in validating some of these conclusions, we demonstrate that the lack of reliable cell segmentation poses a limitation on the type of analyses that can be conducted with this method (Figure S1F). A confounding factor is the likely diffusion of transcripts, which we are confident will be addressed in subsequent versions of this technique or with updated computational methods. We believe that Stereo-seq may prove to be especially valuable when an unbiased profiling of the transcriptome is desired. This may include exploratory analysis that is focused on the broad spatial localization of predefined cell types (or even states) with strongly distinct transcriptomic profiles. Its unbiased nature may also provide valuable insights when performing differential expressions between different conditions, where wider trends between functionally grouped genes can be discerned. However, its potential in brain research will inevitably be limited until adequate cell segmentation can be obtained.

It should be noted that mis-segmentation of transcripts also appears to occur to some extent in the CosMx data, especially for highly expressed transcripts. For example, while we see an expected upregulation of *Gfap* in astrocytes close to

plaques[5,45,46] (Figure 2C), we also see an upregulation of *Gfap* close to plaques in microglia (Figure 2B) that are not known to express this gene. Furthermore, the CosMx technique is inevitably limited by the size of its gene panel, preventing us from reliably assigning previously described cell states.[47]

We propose that the development of DAAs in pathologically severe plaque niches causes neuronal dysfunction in neighboring neurons. This dysfunction leads to a decreased firing of hippocampal CA1–CA3 and DG and may ultimately contribute to the memory deficits.

To validate this hypothesis, the astrocyte uptake of GABA could be tested using GABA sensors, and mice could be treated with Mfg-e8 to demonstrate the reversal of the DAA signature.[20] These experiments would serve as confirmation that hypoactivity in the neurons can be resolved by targeting astrocytic cell states and would provide indications as to whether targeting either the development of DAA or the glial interactions that drive DAA formation could serve as potential therapeutic avenues.

Conclusion

In this study, we characterized the cellular and transcriptomic variations in local amyloid plaque environments through the use of two novel ST methods. We expanded on previously defined cell-type signatures in plaque niches and provide further evidence for microglial-astrocytic crosstalk in these microenvironments. Notably, we extended our analyses beyond glial cell types and characterized the disruptive effects microglial and astrocytic alterations have on neuronal synaptic signaling in the local amyloid plaque environment. We propose that as plaque pathology matures, astrocytic interactions with hippocampal neurons disrupt neuronal signaling through increased inhibitory GABAergic signaling and decreased excitatory glutamatergic signaling. We thus present candidate signaling partners that link the progression of plaque pathology with downstream, detrimental effects on neurons. In parallel, we present a framework of computational approaches and analytical methods with which to probe high-resolution ST datasets.

STAR★METHODS

Detailed methods are provided in the online version of this paper and include the following:

- KEY RESOURCES TABLE
- RESOURCE AVAILABILITY
  - Lead contact
  - Materials availability
  - Data and code availability
- EXPERIMENTAL MODEL AND STUDY PARTICIPANT DETAILS
  - Mice
- METHOD DETAILS
  - Stereo-seq: experimental method
  - CosMx: experimental method
  - IHC staining of adjacent sections
- QUANTIFICATION AND STATISTICAL ANALYSIS
  - Stereo-seq: data processing
  - Image-based single cell segmentation
  - Stereo-seq raw data processing
  - Transcript visualization
  - CosMx: data processing
  - Unsupervised clustering of the cells and bins
  - Amyloid segmentation
  - Calculation of distances to plaques
  - Dimensionality reduction and deconvolution of Stereo-seq plaque niches
  - Plaque niche neighborhood analyses
  - Gene set score calculation
  - Differential gene expression analyses (DE)
  - Gene set enrichment analyses
  - Receptor-ligand analyses
  - Cell type reference

SUPPLEMENTAL INFORMATION

Supplemental information can be found online at https://doi.org/10.1016/j.celrep.2024.114216.

ACKNOWLEDGMENTS

We would like to thank BGI for providing us with access and training to the Stereo-seq platform and for the continued collaboration, as well as VIB Technology Watch member Yu-Chun Wang for facilitating collaborations with BGI research. We would like to thank NanoString for making the CosMx experiment possible through the Technology Access Program and the Francis Crick Institute for funding this experiment. Thanks also goes to Tancredi Massimo Pentimalli, who inspired us to pursue neighborhood analyses by presenting his own CosMx analysis. This work is supported by the UK Dementia Research Institute (award number UK DRI-1004), which receives its funding from UK DRI, Ltd., funded by the UK Medical Research Council, Alzheimer's Society, and Alzheimer's Research UK. In addition, a Medical Research Council Programme Grant (MR/Y014847/1) was awarded to B.D.S. and I.L.A.-C. The work was also funded by an anonymous foundation grant titled "The application of spatial transcriptomics at single-cell resolution in Alzheimer's disease." Work in the Leuven laboratory was supported by funding from the European Research Council (ERC) under the European Union's Horizon 2020 Research and Innovation Programme (grant agreement no. ERC-834682 CELLPHASE_AD). This work was also supported by the Flanders Institute for Biotechnology (VIB vzw), a Methusalem grant from KU Leuven and the Flemish Government, the Fonds voor Wetenschappelijk Onderzoek, KU Leuven, The Queen Elisabeth Medical Foundation for Neurosciences, the Opening the Future campaign of the Leuven Universitair Fonds, The Belgian Alzheimer Research Foundation (SAO-FRA), and the Alzheimer's Association USA. B.D.S. holds the Bax-Vanluffelen Chair for Alzheimer's Disease.

AUTHOR CONTRIBUTIONS

Conceptualization, A.M., M.Z., M.V., W.-T.C., M.F., I.L.A.-C., and B.D.S.; methodology, V.v.L., Y.A., and J.H.K.; software, M.Z., D.M., and M.F.; validation, A.M., M.Z., and V.v.L.; formal analysis, A.M., M.Z., V.v.L., D.M., and M.F.; investigation, V.v.L., Y.A., and J.H.K.; resources, A.M., M.V., W.-T.C., Y.A., and J.H.K.; data curation, M.Z. and M.F.; writing – original draft, A.M., M.Z., and V.v.L.; writing – review & editing, A.M., M.Z., I.L.A.-C., M.F., and B.D.S.; visualization, A.M. and M.Z.; supervision, A.M., M.F., I.L.A.-C., and B.D.S.; project administration, A.M., M.F., I.L.A.-C., and B.D.S.; funding acquisition, A.M., I.L.A.-C., and B.D.S.

DECLARATION OF INTERESTS

B.D.S. has been a consultant for Eli Lilly, Biogen, Janssen Pharmaceutica, Eisai, AbbVie, and other companies and is now consultant to Muna Therapeutics. B.D.S. is a scientific founder of Augustine Therapeutics and a scientific founder and stockholder of Muna Therapeutics. M.F. is a consultant to Muna Therapeutics. Y.A. and J.H.K. are employees of BGI Research, and M.V. and W.T.-C. are employed by Muna Therapeutics. W.T.-C. is also a stockholder of Muna Therapeutics.

Received: June 20, 2023
Revised: February 2, 2024
Accepted: April 25, 2024

REFERENCES

1. De Strooper, B., and Karran, E. (2016). The Cellular Phase of Alzheimer's Disease. Cell *164*, 603–615. https://doi.org/10.1016/j.cell.2015.12.056.
2. Keren-Shaul, H., Spinrad, A., Weiner, A., Matcovitch-Natan, O., Dvir-Szternfeld, R., Ulland, T.K., David, E., Baruch, K., Lara-Astaiso, D., Toth, B., et al. (2017). A Unique Microglia Type Associated with Restricting Development of Alzheimer's Disease. Cell *169*, 1276–1290.e17. https://doi.org/10.1016/j.cell.2017.05.018.
3. Sala Frigerio, C., Wolfs, L., Fattorelli, N., Thrupp, N., Voytyuk, I., Schmidt, I., Mancuso, R., Chen, W.T., Woodbury, M.E., Srivastava, G., et al. (2019). The Major Risk Factors for Alzheimer's Disease: Age, Sex, and Genes Modulate the Microglia Response to Aβ Plaques. Cell Rep. *27*, 1293–1306.e6. https://doi.org/10.1016/j.celrep.2019.03.099.
4. Butovsky, O., and Weiner, H.L. (2018). Microglial signatures and their role in health and disease. Nat. Rev. Neurosci. *19*, 622–635. https://doi.org/10.1038/s41583-018-0057-5.
5. Habib, N., McCabe, C., Medina, S., Varshavsk, M., Kitsberg, D., Dvir-Szternfeld, R., Green, G., Dionne, D., Nguyen, L., Marshall, J.L., et al. (2020). Disease-associated astrocytes in Alzheimer's disease an aging. Nat. Neurosci. *23*, 701–706. https://doi.org/10.1038/s41593-020-06240-8.
6. Liddelow, S.A., Guttenplan, K.A., Clarke, L.E., Bennett, F.C., Bohlen, C.J., Schirmer, L., Bennett, M.L., Münch, A.E., Chung, W.S., Peterson, T.C., et al. (2017). Neurotoxic reactive astrocytes are induced by activated microglia. Nature *541*, 481–487. https://doi.org/10.1038/nature21029.
7. Zamanian, J.L., Xu, L., Foo, L.C., Nouri, N., Zhou, L., Giffard, R.G., and Barres, B.A. (2012). Genomic analysis of reactive astrogliosis. J. Neurosci. *32*, 6391–6410. https://doi.org/10.1523/JNEUROSCI.6221-11.2012.
8. Chen, W.T., Lu, A., Craessaerts, K., Pavie, B., Sala Frigerio, C., Corthout, N., Qian, X., Laláková, J., Kühnemund, M., Voytyuk, I., et al. (2020). Spatial Transcriptomics and In Situ Sequencing to Study Alzheimer's Disease. Cell *182*, 976–991.e19. https://doi.org/10.1016/j.cell.2020.06.038.
9. He, S., Bhatt, R., Brown, C., Brown, E.A., Buhr, D.L., Chantranuvatana, K., Danaher, P., Dunaway, D., Garrison, R.G., Geiss, G., et al. (2022). High-plex imaging of RNA and proteins at subcellular resolution in fixed tissue by spatial molecular imaging. Nat. Biotechnol. *40*, 1794–1806. https://doi.org/10.1038/s41587-022-01483-z.
10. Chen, A., Liao, S., Cheng, M., Ma, K., Wu, L., Lai, Y., Yang, J., Li, W., Xu, J., Hao, S., et al. (2022). Spatiotemporal transcriptomic atlas of mouse organogenesis using DNA nanoball-patterend arrays. Cell *185*, 1777–1792.e21. https://doi.org/10.1101/2021.01.17.427004.
11. Wei, X., Fu, S., Li, H., Liu, Y., Wang, S., Feng, W., Yang, Y., Liu, X., Zeng, Y.-Y., Cheng, M., et al. (2022). Single-cell Stereo-seq reveals induced progenitor cells involved in axolotl brain regeneration. Science *377*, eabp9444. https://doi.org/10.1126/science.abp9444.
12. Massimo Pentimalli, T., Schallenberg, S., León-Periñán, D., Theurillat, I., Thomas, G., Boltengagen, A., Fritzsche, S., Nimo, J., Ruff, L., Dernbach, G., et al. (2023). High-resolution Molecular Atlas of a Lung Tumor in 3D. Preprint at BioRxiv. https://doi.org/10.1101/2023.05.10.539644.
13. Saito, T., Matsuba, Y., Mihira, N., Takano, J., Nilsson, P., Itohara, S., Iwata, N., and Saido, T.C. (2014). Single App knock-in mouse models of Alzheimer's disease. Nat. Neurosci. *17*, 661–663. https://doi.org/10.1038/nn.3697.
14. Yao, Z., van Velthoven, C.T.J., Nguyen, T.N., Goldy, J., Sedeno-Cortes, A.E., Baftizadeh, F., Bertagnolli, D., Casper, T., Chiang, M., Crichton, K., et al. (2021). A taxonomy of transcriptomic cell types across the isocortex and hippocampal formation. Cell *184*, 3222–3241.e26. https://doi.org/10.1016/j.cell.2021.04.021.
15. Batiuk, M.Y., Martirosyan, A., Wahis, J., de Vin, F., Marneffe, C., Kusserow, C., Koeppen, J., Viana, J.F., Oliveira, J.F., Voet, T., et al. (2020). Identification of region-specific astrocyte subtypes at single cell resolution. Nat. Commun. *11*, 1220. https://doi.org/10.1038/s41467-019-14198-8.
16. Efremova, M., Vento-Tormo, M., Teichmann, S.A., and Vento-Tormo, R. (2020). CellPhoneDB: inferring cell–cell communication from combined expression of multi-subunit ligand–receptor complexes. Nat. Protoc. *15*, 1484–1506. https://doi.org/10.1038/s41596-020-0292-x.
17. Dai, D.L., Li, M., and Lee, E.B. (2023). Human Alzheimer's disease reactive astrocytes exhibit a loss of homeostastic gene expression. Acta Neuropathol. Commun. *11*, 127. https://doi.org/10.1186/s40478-023-01624-8.
18. Kleshchevnikov, V., Shmatko, A., Dann, E., Aivazidis, A., King, H.W., Li, T., Elmentaite, R., Lomakin, A., Kedlian, V., Gayoso, A., et al. (2022). Cell2location maps fine-grained cell types in spatial transcriptomics. Nat. Biotechnol. *40*, 661–671. https://doi.org/10.1038/s41587-021-01139-4.
19. Sadick, J.S., O'Dea, M.R., Hasel, P., Dykstra, T., Faustin, A., and Liddelow, S.A. (2022). Astrocytes and oligodendrocytes undergo subtype-specific transcriptional changes in Alzheimer's disease. Neuron *110*, 1788–1805.e10. https://doi.org/10.1016/j.neuron.2022.03.008.
20. Xu, X., Zhang, A., Zhu, Y., He, W., Di, W., Fang, Y., and Shi, X. (2018). MFG-E8 reverses microglial-induced neurotoxic astrocyte (A1) via NF-κB and PI3K-Akt pathways. J. Cell. Physiol. *234*, 904–914. https://doi.org/10.1002/jcp.26918.
21. Hébert, S.S., Horré, K., Nicolaï, L., Papadopoulou, A.S., Mandemakers, W., Silahtaroglu, A.N., Kauppinen, S., Delacourte, A., and De Strooper, B. (2008). Loss of microRNA cluster miR-29a/b-1 in sporadic Alzheimer's disease correlates with increased BACE1/β-secretase expression. Proc. Natl. Acad. Sci. USA *105*, 6415–6420. https://doi.org/10.1073/pnas.0710263105.
22. Shioya, M., Obayashi, S., Tabunoki, H., Arima, K., Saito, Y., Ishida, T., and Satoh, J. (2010). Aberrant microRNA expression in the brains of neurodegenerative diseases: MiR-29a decreased in Alzheimer disease brains targets neurone navigator 3. Neuropathol. Appl. Neurobiol. *36*, 320–330. https://doi.org/10.1111/j.1365-2990.2010.01076.x.
23. Azargoonjahromi, A. (2023). Dual Role of Nitric Oxide in Alzheimer's Disease. Nitric Oxide. https://doi.org/10.1016/j.niox.2023.03.
24. Chakroborty, S., Kim, J., Schneider, C., West, A.R., and Stutzmann, G.E. (2015). Nitric oxide signaling is recruited as a compensatory mechanism for sustaining synaptic plasticity in Alzheimer's disease mice. J. Neurosci. *35*, 6893–6902. https://doi.org/10.1523/JNEUROSCI.4002-14.2015.
25. Zeng, H., Huang, J., Zhou, H., Meilandt, W.J., Dejanovic, B., Zhou, Y., Bohlen, C.J., Lee, S.-H., Ren, J., Liu, A., et al. (2023). Integrative in situ mapping of single-cell transcriptional states and tissue histopathology in an Alzheimer's disease model. Nat. Neurosci. *26*, 430–446. https://doi.org/10.1101/2022.01.14.476072.
26. Clarke, L.E., Liddelow, S.A., Chakraborty, C., Münch, A.E., Heiman, M., and Barres, B.A. (2018). Normal aging induces A1-like astrocyte reactivity. Proc. Natl. Acad. Sci. USA *115*, E1896–E1905. https://doi.org/10.1073/pnas.1800165115.
27. Hasel, P., Rose, I.V.L., Sadick, J.S., Kim, R.D., and Liddelow, S.A. (2021). Neuroinflammatory astrocyte subtypes in the mouse brain. Nat. Neurosci. *24*, 1475–1487. https://doi.org/10.1038/s41593-021-00905-6.
28. Deczkowska, A., Keren-Shaul, H., Weiner, A., Colonna, M., Schwartz, M., and Amit, I. (2018). Disease-Associated Microglia: A Universal Immune Sensor of Neurodegeneration. Cell *173*, 1073–1081. https://doi.org/10.1016/j.cell.2018.05.003.

29. Spangenberg, E., Severson, P.L., Hohsfield, L.A., Crapser, J., Zhang, J., Burton, E.A., Zhang, Y., Spevak, W., Lin, J., Phan, N.Y., et al. (2019). Sustained microglial depletion with CSF1R inhibitor impairs parenchymal plaque development in an Alzheimer's disease model. Nat. Commun. *10*, 3758. https://doi.org/10.1038/s41467-019-11674-z.

30. Wang, C., Xiong, M., Gratuze, M., Bao, X., Shi, Y., Andhey, P.S., Manis, M., Schroeder, C., Yin, Z., Madore, C., et al. (2021). Selective removal of astrocytic APOE4 strongly protects against tau-mediated neurodegeneration and decreases synaptic phagocytosis by microglia. Neuron *109*, 1657–1674.e7. https://doi.org/10.1016/j.neuron.2021.03.024.

31. Kersanté, F., Rowley, S.C.S., Pavlov, I., Gutièrrez-Mecinas, M., Semyanov, A., Reul, J.M.H.M., Walker, M.C., and Linthorst, A.C.E. (2013). A functional role for both γ-aminobutyric acid (GABA) transporter-1 and GABA transporter-3 in the modulation of extracellular GABA and GABAergic tonic conductances in the rat hippocampus. J. Physiol. *591*, 2429–2441. https://doi.org/10.1113/jphysiol.2012.246298.

32. Liu, J., Feng, X., Wang, Y., Xia, X., and Zheng, J.C. (2022). Astrocytes: GABAceptive and GABAergic Cells in the Brain. Front Cell Neurosci. https://doi.org/10.3389/fncel.2022.892497.

33. Brawek, B., Chesters, R., Klement, D., Müller, J., Lerdkrai, C., Hermes, M., and Garaschuk, O. (2018). A bell-shaped dependence between amyloidosis and GABA accumulation in astrocytes in a mouse model of Alzheimer's disease. Neurobiol. Aging *61*, 187–197. https://doi.org/10.1016/j.neurobiolaging.2017.09.028.

34. Jo, S., Yarishkin, O., Hwang, Y.J., Chun, Y.E., Park, M., Woo, D.H., Bae, J.Y., Kim, T., Lee, J., Chun, H., et al. (2014). GABA from reactive astrocytes impairs memory in mouse models of Alzheimer's disease. Nat. Med. https://doi.org/10.1038/nm.3639.

35. Magnin, E., Francavilla, R., Amalyan, S., Gervais, E., David, L.S., Luo, X., and Topolnik, L. (2019). Input-specific synaptic location and function of the α5 GABA a receptor subunit in the mouse CA1 hippocampal neurons. J. Neurosci. *39*, 788–801. https://doi.org/10.1523/JNEUROSCI.0567-18.2018.

36. Kwakowsk, A., Calvo-Flores Guzman, B., Pandya, M., Turner, C., Waldvogel, H.J., and Faull, R.L. (2018). GABAA receptor subunit expression changes in the human Alzheimer's disease hippocampus, subiculum, entorhinal cortex and superior temporal gyrus. J. Neurochem. *145*. https://doi.org/10.1111/jnc.14179.

37. Jacob, C.P., Koutsilieri, E., Bartl, J., Neuen-Jacob, E., Arzberger, T., Zander, N., Ravid, R., Roggendorf, W., Riederer, P., and Grünblatt, E. (2007). Alterations in Expression of Glutamatergic Transporters and Receptors in Sporadic Alzheimer's Disease. J. Alzheimers Dis. *11*, 97–116. https://doi.org/10.3233/JAD-2007-11113.

38. Mookherjee, P., Green, P.S., Watson, G.S., Marques, M.A., Tanaka, K., Meeker, K.D., Meabon, J.S., Li, N., Zhu, P., Olson, V.G., and Cook, D.G. (2011). GLT-1 Loss Accelerates Cognitive Deficit Onset in an Alzheimer's Disease Animal Model. J. Alzheimers Dis. *26*, 447–455. https://doi.org/10.3233/JAD-2011-110503.

39. Bereczki, E., Branca, R.M., Francis, P.T., Pereira, J.B., Baek, J.-H., Hortobagyi, T., Winblad, B., Ballard, C., Lehtio, J., and Aarsland, D. (2018). Synaptic Markers of Cognitive Decline in Neurodegenerative Diseases: A Proteomic Approach. Brain. https://doi.org/10.1093/brain/awx360.

40. Gazestani, V., Kamath, T., Nadaf, N.M., Dougalis, A., Burris, S.J., Rooney, B., Junkkari, A., Vanderburg, C., Pelkonen, A., Gomez-Budia, M., et al. (2023). Early Alzheimer's disease pathology in human cortex involves transient cell states. Cell *186*, 4438–4453.e23. https://doi.org/10.1016/j.cell.2023.08.005.

41. Shah, D., Gsell, W., Wahis, J., Luckett, E.S., Jamoulle, T., Vermaercke, B., Preman, P., Moechars, D., Hendrickx, V., Jaspers, T., et al. (2022). Astrocyte calcium dysfunction causes early network hyperactivity in Alzheimer's disease. Cell Rep. *40*, 111280. https://doi.org/10.1016/j.celrep.2022.111280.

42. Calafate, S., Özturan, G., Thrupp, N., Vanderlinden, J., Santa-Marinha, L., Morais-Ribeiro, R., Ruggiero, A., Bozic, I., Rusterholz, T., Lorente-Echeverría, B., et al. (2023). Early alterations in the MCH system link aberrant neuronal activity and sleep disturbances in a mouse model of Alzheimer's disease. Nat. Neurosci. *26*, 1021–1031. https://doi.org/10.1038/s41593-023-01325-4.

43. Browaeys, R., Saelens, W., and Saeys, Y. (2020). NicheNet: modeling intercellular communication by linking ligands to target genes. Nat. Methods *17*, 159–162. https://doi.org/10.1038/s41592-019-0667-5.

44. Fischer, D.S., Schaar, A.C., and Theis, F.J. (2023). Modeling intercellular communication in tissues using spatial graphs of cells. Nat. Biotechnol. *41*, 332–336. https://doi.org/10.1038/s41587-022-01467-z.

45. Nagele, R.G., D'Andrea, M.R., Lee, H., Venkataraman, V., and Wang, H.Y. (2003). Astrocytes accumulate Aβ42 and give rise to astrocytic amyloid plaques in Alzheimer disease brains. Brain Res. *971*, 197–209. https://doi.org/10.1016/S0006-8993(03)02361-8.

46. Srinivasan, R., Lu, T.Y., Chai, H., Xu, J., Huang, B.S., Golshani, P., Coppola, G., and Khakh, B.S. (2016). New Transgenic Mouse Lines for Selectively Targeting Astrocytes and Studying Calcium Signals in Astrocyte Processes In Situ and In Vivo. Neuron *92*, 1181–1195. https://doi.org/10.1016/j.neuron.2016.11.030.

47. Mancuso, R., Fattorelli, N., Martinez-Muriana, A., Davis, E., Wolfs, L., Van Den Daele, J., Geric, I., Premereur, J., Polanco, P., Bijnens, B., et al. (2024). Xenografted human microglia display diverse transcriptomic states in response to Alzheimer's disease-related amyloid-β pathology. Nat. Neurosci. https://doi.org/10.1038/s41593-024-01600-y.

48. Stringer, C., Wang, T., Michaelos, M., and Pachitariu, M. (2021). Cellpose: a generalist algorithm for cellular segmentation. Nat. Methods *18*, 100–106. https://doi.org/10.1038/s41592-020-01018-x.

49. Schneider, C.A., Rasband, W.S., and Eliceiri, K.W. (2012). NIH Image to ImageJ: 25 years of image analysis. Nat. Methods *9*, 671–675. https://doi.org/10.1038/nmeth.2089.

50. Dobin, A., Davis, C.A., Schlesinger, F., Drenkow, J., Zaleski, C., Jha, S., Batut, P., Chaisson, M., and Gingeras, T.R. (2013). STAR: Ultrafast universal RNA-seq aligner. Bioinformatics *29*, 15–21. https://doi.org/10.1093/bioinformatics/bts635.

51. Van Der Walt, S., Schönberger, J.L., Nunez-Iglesias, J., Boulogne, F., Warner, J.D., Yager, N., Gouillart, E., and Yu, T. (2014). Scikit-image: Image processing in python. PeerJ *2014*. https://doi.org/10.7717/peerj.453.

52. Solorzano, L., Partel, G., and Wählby, C. (2020). TissUUmaps: Interactive visualization of large-scale spatial gene expression and tissue morphology data. Bioinformatics *36*, 4363–4365. https://doi.org/10.1093/bioinformatics/btaa541.

53. Palla, G., Spitzer, H., Klein, M., Fischer, D., Schaar, A.C., Kuemmerle, L.B., Rybakov, S., Ibarra, I.L., Holmberg, O., Virshup, I., et al. (2022). Squidpy: a scalable framework for spatial omics analysis. Nat. Methods *19*, 171–178. https://doi.org/10.1038/s41592-021-01358-2.

54. Wolf, F.A., Angerer, P., and Theis, F.J. (2018). SCANPY: Large-scale single-cell gene expression data analysis. Genome Biol. *19*, 15. https://doi.org/10.1186/s13059-017-1382-0.

55. Bankhead, P., Loughrey, M.B., Fernández, J.A., Dombrowski, Y., McArt, D.G., Dunne, P.D., McQuaid, S., Gray, R.T., Murray, L.J., Coleman, H.G., et al. (2017). QuPath: Open source software for digital pathology image analysis. Sci. Rep. *7*, 16878. https://doi.org/10.1038/s41598-017-17204-5.

56. Virtanen, P., Gommers, R., Oliphant, T.E., Haberland, M., Reddy, T., Cournapeau, D., Burovski, E., Peterson, P., Weckesser, W., Bright, J., et al. (2020). SciPy 1.0: fundamental algorithms for scientific computing in Python. Nat. Methods *17*, 261–272. https://doi.org/10.1038/s41592-019-0686-2.

57. Korsunsky, I., Millard, N., Fan, J., Slowikowski, K., Zhang, F., Wei, K., Baglaenko, Y., Brenner, M., Loh, P.R., and Raychaudhuri, S. (2019). Fast, sensitive and accurate integration of single-cell data with Harmony.

Nat. Methods *16*, 1289–1296. https://doi.org/10.1038/s41592-019-0619-0.

58. Robinson, M.D., McCarthy, D.J., and Smyth, G.K. (2010). edgeR: A Bioconductor package for differential expression analysis of digital gene expression data. Bioinformatics *26*, 139–140. https://doi.org/10.1093/bioinformatics/btp616.

59. Wu, T., Hu, E., Xu, S., Chen, M., Guo, P., Dai, Z., Feng, T., Zhou, L., Tang, W., Zhan, L., et al. (2021). clusterProfiler 4.0: A universal enrichment tool for interpreting omics data. Innovation *2*, 100141. https://doi.org/10.1016/j.xinn.2021.100141.

60. Lein, E.S., Hawrylycz, M.J., Ao, N., Ayres, M., Bensinger, A., Bernard, A., Boe, A.F., Boguski, M.S., Brockway, K.S., Byrnes, E.J., et al. (2007). Genome-wide atlas of gene expression in the adult mouse brain. Nature *445*, 168–176. https://doi.org/10.1038/nature05453.

61. Wolock, S.L., Lopez, R., and Klein, A.M. (2019). Scrublet: Computational Identification of Cell Doublets in Single-Cell Transcriptomic Data. Cell Syst. *8*, 281–291.e9. https://doi.org/10.1016/j.cels.2018.11.005.

62. Xie, Z., Li, X., and Mora, A. (2023). A Comparison of Cell-Cell Interaction Prediction Tools Based on scRNA-seq Data. Biomolecules *13*, 1211. https://doi.org/10.3390/biom13081211.

STAR★METHODS

KEY RESOURCES TABLE

REAGENT or RESOURCE	SOURCE	IDENTIFIER
Antibodies		
GFAP	Synaptic Systems	Cat: 173004; RRID: AB_10641162
MOAB-2	Abcam	Cat: ab126649; RRID: AB_3095985
Goat anti-guinea pig Alexa 568	Invitrogen	Cat: A11075; RRID: AB_2534119
6E10 conjugated with Alexa 488	Biolegend	Cat: 803013; RRID: AB_2564765
Chemicals, peptides, and recombinant proteins		
Methanol	Acros Organics	2170955
ssDNA assay kit	Qubit	Q10212
DAPI	Sigma	D9542
Paraformaldehyde	Thermo Scientific	199077
5% donkey serum	Jackson Immunolabs	017-000-121
PBS	Gibco - ThermoFisher	2293633
Triton X-	Sigma-Aldrich	BCCF3162
1x TrueBlack	Biotium	23007
Ethanol	Fisher Chemical	2351404
SSC buffer	Sigma-Aldrich	SLCJ5290
Glycerol	Acros Organics	1528302
Critical commercial assays		
Stereo-Seq S1 kit	BGI	1000028496
Stereo-Seq Gene expression chip	BGI	1000028497
Stereo-Seq Library Prep kit	BGI	1000028498
Fresh frozen slide preparation kit	Nanostring	121500007
CosMx mouse Neuroscience RNA Probe Mix	Nanostring	121500003
CosMx Mouse Neuroscience Cell segmentation kit	Nanostring	121500024
CosMx Mouse Neuroscience Supplemental segmentation kit	Nanostring	121500025
Deposited data		
Allen brain reference atlas	Yao et al., 2021[14]	https://portal.brain-map.org/atlases-and-data/rnaseq/mouse-whole-cortex-and-hippocampus-10x
Microglia gene signature	Frigerio et al., 2019[3]	GEO: GSE127893
Astrocyte gene signature	Habib et al., 2020[5]	GEO: GSE143758
Raw data and count matrices from spatial transcriptomics	This paper	GEO: GSE263793
Experimental models: Organisms/strains		
App NL-G-F	Saito et al., 2014[13]	Available from the Saido lab.
C57BL/6J	Janvier	C57BL/6JRj
Software and algorithms		
Cellpose	Stringer et al., 2021[48]	github.com/mouseland/cellpose
ImageJ	NIH[49]	https://imagej.nih.gov/ij/
SAW pipeline	BGI	github.com/BGIResearch/SAW
STAR	Dobin et al., 2012[50]	github.com/alexdobin/STAR
Scikit-image	Van der Walt et al., 2014[51]	github.com/scikit-image/scikit-image

(*Continued on next page*)

Continued

REAGENT or RESOURCE	SOURCE	IDENTIFIER
rearrr	Ludvig R. Olsen	github.com/LudivfOlsen/rearrr
stereopy	BGI	github.com/BGIResearch/stereopy
TissUUmaps	Solorzano et al., 2020[52]	github.com/wahlby-lab/TissUUmaps
squidpy	Palla et al., 2022[53]	github.com/theislab/squidpy
scanpy	Wolf et al., 2018[54]	github.com/scverse/scanpy
QuPath	Bankhead et al., 2017[55]	https://qupath.github.io/
Scipy	Virtanen et al., 2020[56]	github.com/scipy/scipy
Harmony	Korsunsky et al., 2019[57]	github.com/immunogenomics/harmony
Cell2location	Kleshchevnikov et al., 2022[18]	github.com/BayraktarLab/cell2location
EdgeR	Robinson et al., 2010[58]	bioconductor.org/packages/release/bioc/html/edgeR.html
clusterProfiler	Wu et al., 2021[59]	github.com/YuLab-SMU/clusterProfiler
CellPhoneDB	Efremova et al., 2020[16]	github.com/Teichlab/cellphonedb

RESOURCE AVAILABILITY

Lead contact

Further information and requests for resources and reagents should be directed to and will be fulfilled by the lead contact, Professor Bart De Strooper.

Materials availability

This study did not generate new unique reagents.

Data and code availability

- The spatial data (including imaging, raw sequencing, and expression data), have been deposited at GEO and are publicly available as of the date of publication. The accession number is listed in the key resources table. Microscopy images will be shared by the lead contact upon request.
- This paper does not report original code.
- Further information and requests for data analysis and data availability should be directed to and will be fulfilled by Professor Mark Fiers. Any additional information required to re-analyze the data reported in this paper is available upon request.

EXPERIMENTAL MODEL AND STUDY PARTICIPANT DETAILS

Mice

All animal experiments were conducted in line with approved protocols by the Ethical Committee of Laboratory Animals of the KU Leuven. Male mice containing the *App*$^{NL\text{-}G\text{-}F}$ knock-in mutation[13] expressed *App* mutations in the C57BL/6J background were used due to the previously shown sex differences in this animal model.[3] Mice were housed with *ad libitum* access to food and water and a 14-h light/10 h dark cycle at 21°C. The *App*$^{NL\text{-}G\text{-}F}$ model contains the humanized Aβ sequence, as well as Swedish (NL), Arctic (G), and Iberian (F) mutations and has been shown to accumulate Aβ pathology and to suffer from cognitive impairment from the age of 6 months onwards,[13] making it a relevant model for our interest in the local environment around plaques. For spatial transcriptomic and single cell experiments, we prefer a mouse model that expresses APP from the endogenous promoter, as it reduces artifacts caused by over-expression or off-target processing. For spatial transcriptomic experiments, *App*$^{NL\text{-}G\text{-}F}$ mice and wildtype (WT) controls were sacrificed at 3 months (3M) and 18 months (18M) using a carbon dioxide overdose. Following cervical dislocation, left and right hemispheres were embedded in cold OCT and snap-frozen in isopentane chilled with liquid nitrogen and stored at −80°C.

METHOD DETAILS

Stereo-seq: experimental method

For Stereo-seq, 10 μm thick tissue sections were adhered to the Stereo-seq chip and incubated at 37°C for 3 min,[10] with immediately adjacent slides collected for staining. The sections were fixed in methanol for 30 min at −20°C. The sections were then stained for ssDNA and imaged to obtain nuclei location information. Tissue sections were then permeabilized for 12 min and reverse transcription performed overnight at 42°C. Afterward, tissue was digested and cDNA released from the chip. The recovered cDNA was amplified and a total of 20ng was fragmented for library construction. PCR products were purified and sequenced on an MGI DNBSEQ-Tx

sequencer. Two mixed hemispheres, where one hemisphere is from a WT mouse and the other from an *App*$^{NL-G-F}$ mouse, were processed for 3M animals, whilst two full coronal sections were processed for the 18M *App*$^{NL-G-F}$ mice, with one full coronal section of an age-matched control.

CosMx: experimental method

10 μm thick tissue sections were collected and fixed.[9] Following the kit, target retrieval was performed followed by a tissue digestion for 30 min at room temperature. *In situ* hybridisation was performed with the RNA mouse neuroscience panel, including the 18s RNA probe, and antibody morphology stain was performed with the cell segmentation kit at a dilution of 1:25, staining for histone, glial fibrillary acidic protein (GFAP), 4′,6-diamidino-2-phenylindole (DAPI). In addition, MOAB-2 (1:25 dilution) was used to stain for amyloid-β. Information from 84 FOV, with each FOV the size of 510 μm × 510 μm, were analyzed. After data acquisition, decoding of individual transcripts and segmentation of cells, based on Cellpose,[48] was performed.[9] Data was acquired from four coronal sections of 18M hemispheres of an *App*$^{NL-G-F}$ mouse.

IHC staining of adjacent sections

Adjacent slides from the Stereo-seq experiments were stained using a standard IHC protocol to visualize reactive astrocytes and amyloid-β plaques. In brief, after fixation with 4% paraformaldehyde for 10 min and 90 min incubation with a blocking solution (5% donkey serum and 0.5% Triton X-, in PBS) at room temperature, the tissue sections were incubated with GFAP antibody (1:500 dilution) and anti-amyloid-β 3–8 (6E10) antibody conjugated with fluorophore Alexa 488 (1:200 dilution) overnight at 4°C. The following day, sections were incubated with appropriate secondary antibodies (Goat anti-Guinea Pig Alexa 568, 1:200 dilution) for 90 min at room temperature. After five wash steps, autofluorescence was quenched by treating sections for 30 s with 1x TrueBlack solution diluted in 70% ethanol. Afterward, the sections were rinsed by dipping the slides 20x in PBS. Nuclei were visualized by incubating the sections with DAPI staining for 15 min at room temperature. Sections were rinsed in SSC buffer, before 100 μL glycerol was added and a coverslip was applied.

16-bit fluorescent images of DAPI, 6E10, and GFAP were acquired on a Zeiss Axioscan.Z1 slidescanner, with a 20x/0.8 NA air objective using the ZEN blue software (version 3.1, Carl Zeiss Microscopy GmbH). Different FOV were stitched together using the online stitching configuration in the software.

QUANTIFICATION AND STATISTICAL ANALYSIS

All details on the number of subjects and samples can be found in the results section and corresponding figure legends. Where appropriate, normality was assessed using the Shapiro-Wilk test and appropriate nonparametric tests were used where the assumption of normality was not met. For correlation analyses, Pearson correlations were used unless stated otherwise.

Stereo-seq: data processing

The Stereo-seq raw data processing was performed using the publicly available SAW pipeline (https://github.com/BGIResearch/SAW).[10] fastq files were generated using an MGI DNBSEQ-Tx sequencer. CID sequences (1–25 bp) on the first reads were first mapped to the designed coordinates of the *in situ* captured chip, allowing 1 base mismatch. Low quality reads were filtered out, and retained reads were aligned to the mm10 reference genome using STAR.[50] Mapped reads with MAPQ >10 were counted and annotated to their corresponding genes. UMIs with the same CID and the same gene locus were collapsed, again allowing 1 base mismatch, resulting in a CID-containing expression profile matrix.

Image-based single cell segmentation

Single cell segmentation was performed by first aligning the nucleic acid staining to the Stereo-seq chips and then applying the watershed algorithm through the Scikit-image package (V0.18.1). The number of markers required for the watershed algorithm were obtained through Gaussian-weighted local threshold binarization with block size of 41 and offset of 0.003. We then exacted Euclidean distance transformation (with distance of 13 or 15) from the background removed images. For each of the segmented cells, UMIs from all DNB within the corresponding segmentation were aggregated per-gene and then summed to generate a cell by gene matrix. The centroid of each cell was determined using rearrr (https://github.com/LudvigOlsen/rearrr).

Stereo-seq raw data processing

Gem files specifying the X/Y coordinates and MID count for every DNB were read in using stereopy's read_gem() (https://github.com/BGIResearch/stereopy) to generate both a bin20 expression matrix (with argument bin_size = 20) and a cell_bin expression matrix (argument bin_type = 'cell_bins'). Both datasets were manually aligned with 13 brain regions defined by the Allen Brain Mouse Atlas,[60] and each cell/bin was assigned to a region (Figure S1D). Cells/bins overlapping with white matter and with the cerebral nuclei region were removed. The 13 brain regions were further grouped into 5 coarse regions (brain stem, cortical subplate, hippocampus, isocortex, and olfactory bulb). To then remove low-quality bins, bins with a high or a low number of genes, MIDs, mitochondrial content were removed. Furthermore, genes expressed in less than 0.1% of bins in a given sample were removed. A total of 2,425,202 high-quality bin20s across all 5 tissue sections were retained for subsequent analysis.

Transcript visualization

Visualization of spatial localization of Stereo-seq transcripts, overlaid over segmented plaque images, was performed using TissUUmaps (v3.0.10).[52] In brief, the bin1 gem file for an 18M *App*$^{NL-G-F}$ mouse was uploaded in the *"Markers"* tab of the TissUUmaps interface, run on a local server. Selected PIG transcripts (*Trem2, Hexb, Tyrobp, Ctsd,* and *Lyz2*) were selected for visualization. The corresponding aligned amyloid plaque mask was uploaded in the "*Image Layers*" tab, allowing for an overlay of the selected transcripts over the plaque mask.

CosMx: data processing

The expression matrices, metadata, and FOV files for the four *App*$^{NL-G-F}$ tissue sections were read in using squidpy's *read_nanostring()* function. Transcripts associated with negative probes were removed from the count matrices. Cells were manually assigned regional annotation based on visual alignment with the Allen Brain Mouse Atlas reference (Figure S1C). Cells with a high or low number of genes or transcripts were removed. In order to identify likely mis-segmented doublets (i.e., two cells that were incorrectly identified as one cell during the segmentation process), scrublet[61] was run on each of the hippocampal sections, separately. Cells that were assigned a high doublet probability were removed.

To account for potential non-specific binding of probes to amyloid plaques, we analyzed the expression level of each gene, including the negative probes, within a cell overlapping with a plaque and correlated it to the plaque overlap. We found that particularly two negative probes showed a strong correlation (R2 = 0.65 for NegPrb1 and R2 = 0.47 for NegPrb7), indicating non-specific binding of probes and arguably also genes, to plaques. We discarded all transcripts that had a higher correlation than the top two negative probes (for a total of 56 probes) from further analysis, as likely candidates of nonspecific binding. To remove cells that may have still been contaminated with, we subclustered the microglial cells, identified a cluster of cells characterized by higher counts of negative probe counts, and removed this cluster (141 cells) from subsequent analysis. A total of 37,840 high-quality cells across all tissue sections were retained for subsequent analysis.

Unsupervised clustering of the cells and bins

Cells/bins passing quality control in each of the datasets were further processed using the SCANPY workflow. Raw gene expression counts were first log-transformed and normalized by library size using the *normalize_total()* and *log1p()* functions, and subsequently scaled to unit variance and zero mean with the *scale()* function. Principal Component Analysis (PCA) was performed on the expression profile of the genes. Cells/bins from different Stereo-seq chips were integrated using Harmony[57] to account for inter-chip batch effects. The first 20 PCs were used as input for dimensionality reduction with Uniform Manifold Approximation and Projection (UMAP). CosMx cells were clustered using the Leiden method at a resolution of 0.45 to obtain 15 clusters and did not require integration (Figure S1B). Clusters were annotated for cell type based on relative expression of cell type marker genes, (determined with the *score_genes()* function). The subclusters characterizing the glutamatergic neuron cluster were further annotated based on their regional spatial distribution.

Amyloid segmentation

Amyloid-β plaques were annotated using the QuPath software through a pixel classification threshold with an additional size threshold of 65,000 px to discriminate the pathology from background and artificial staining. The segmentation was then manually checked to ensure segmented plaques were of high quality. The segmented plaques were then exported to ImageJ and converted into a binary mask for alignment to the transcriptome.

Using a previously described technique, the adjacent slide staining was aligned to the transcriptome of the Stereo-seq chip through the selection of corresponding landmarks on both the staining and the transcriptome.[8] Using the Fiji "Landmark correspondences" plugin, the staining was then aligned to overlay with the transcriptome. The same method was followed for alignment of the Allen Brain Atlas with the transcriptome that allowed for assignment of brain regions to the transcriptome (Figures S1C and S1D). After alignment of adjacent slide stainings, segmented masks from either side of each chip were summed to obtain one binary amyloid segmentation mask per chip.

Calculation of distances to plaques

The distance from the center of each bin/cell to the edge of the nearest segmented plaque was calculated using Scipy's KDTree package: (https://github.com/scipy/scipy/blob/main/scipy/spatial/kdtree.py).

Dimensionality reduction and deconvolution of Stereo-seq plaque niches

The transcriptomic profiles of plaque niches in the Stereo-seq dataset were acquired by "pseudo-bulking" all the transcripts identified within 40 μm (80 pixels) from the edge of a plaque, inclusive of those overlaying the plaque. Processing of the pseudobulked niches was performed using SCANPY. Plaque niches with less than 10 transcripts, as well as lowly expressed genes, were discarded from further analysis, resulting in a total of $n = 4,285$ analyzed plaque niches. The resultant expression matrix was log-normalized to a scale factor of 10,000 and total transcript counts were regressed. Principal Component Analysis (PCA) was performed, and the niches were integrated across samples using Harmony.[57] The first 10 principal components were used to construct the UMAP and a resolution of 0.3 was used to cluster the niches. Cell2location was then used to infer the cellular composition of these

pseudo-bulked plaque niches, using the scRNA-seq dataset from the Allen Brain Mouse Atlas[14] as the reference dataset. The single-cell reference dataset was first filtered using *filter_genes(),* with the parameters cell_count_cutoff = 5, cell_percentage_cutoff2 = 0.03, nonz_mean_cutoff = 1.12. The regression model for the reference data was initialized with default settings. The model was then trained using a maximum of 1,000 epochs. Reference and spatial datasets were filtered for shared genes. The inferred reference cell type signatures were then used for spatial cell-type mapping, using the hyperparameters N_cells_per_location = 30 and detection_alpha = 15. The cell2location model was trained on the full data using 15,000 epochs, and the cell abundance estimations were extracted.

Plaque niche neighborhood analyses

Plaque x cell type density matrices were created by counting, for every plaque, the number of each given cell type lying within a 40 μm distance (80 pixels in Stereo-seq, 240 pixels in CosMx) from the plaque's edge and dividing that number by the total number of cells within that radius. In the case of the CosMx dataset, segmented cells were counted, only taking plaques into consideration that contained 5 or more cells. For Stereo-seq, cell type compositions inferred by cell2location were used. The resultant matrices were used for dimensionality reduction in SCANPY, using the *sc.tl.pca()*, *sc.pp.neighbors()*, and *sc.tl.umap()* functions.

Gene set score calculation

To obtain gene set scores of plaque niches and cells in Stereo-seq and CosMx, respectively, the PNs and cells were log-normalized to a scale factor of 10,000 and scored on their relative expression of relevant gene sets (i.e., DAM marker genes, HM marker genes,[3] DAA markers, and homeostatic astrocyte markers[5]) using SCANPY's *score_genes()* function. The DAM scores of CosMx plaque niches were taken as the max DAM score of any microglia in the given plaque niche.

Differential gene expression analyses (DE)

DE analyses were conducted by fitting generalized linear models (GLM), using either distance to plaque pathology or plaque niche microglial density as the continuous covariate of interest. This allows to capture the full extent of the changes and to not limit the analysis to specific binary comparisons that require arbitrary cut-offs (such as cells within 10 μm from pathology in comparison with cells further away). Each GLM model was tested for DE with EdgeR's quasi-likelihood F-test (QLFTest) which accounts for the uncertainty in dispersion estimation. DEs with respect to distance to pathology were performed with respect to log1p(d), with d being the distance from the cell/bin centroid to the plaque centroid for both CosMx and Stereo-seq. This model therefore represents transcriptional changes of a cell/bin as it nears a plaque. The microglial density model represents the transcriptional changes in gene expression per additional microglial density in the cell's respective plaque niche. Multiplicity correction was performed by applying the Benjamini-Hochberg (BH) method on the associated p-values, and a significance threshold of p.adj <0.05 was used for all DEs. DEs in the CosMx dataset were performed on individual cells on a cell-type basis, limiting the analysis to only the cell type markers for the given cell type. Cell type markers were obtained by running differential expressions between all clusters (i.e., cell types) using SCANPY's *rank_genes_groups()* function, and filtering for genes that were significantly differentially expressed at a p.adj >0.05 and log2FC > 0.5.

Gene set enrichment analyses

Gene set enrichment analyses (GSEA) were performed using R's clusterProfiler package,[59] using the log2 fold change value for gene rank. The associated p-value was calculated based on the permutation-generated null distribution, and it reflects the probability under the null distribution of obtaining an enrichment score value that is at least as strong as that observed for the random permutations.

Receptor-ligand analyses

To analyze RL pairs between microglia and astrocytes as they approach plaques, we ran CellPhoneDB,[16] because of its high specificity and precision compared to other algorithms.[62] We ran this algorithm on all hippocampal cells using the "cpdb_degs_analysis_method", limiting the predicted RL pairs to any gene that was differentially expressed with regards to distance to plaques (see *Methods: Differential gene expression analyses)* and to any gene that is expressed in more than 10% of the cells of a given cell type. The identified RL pairs were limited to pairs that contained at least one gene that was previously identified as PIG. To analyze changes in the plaque niches with regards to microglial density, we followed a similar approach as above, analyzing only cells present in hippocampal plaque niches and limiting the RL pairs to pairs where at least one partner is predicted to be differentially expressed in the cell type with regards to microglial density of the plaque niche.

The number of RL pairs for each combination of cell type was generated by counting the number of significant RL pairs and in the second step, normalizing this to the total number of genes that the differential gene expression was performed on.

For the co-occurrence analysis, we took the significant RL pairs generated from CellPhoneDB and analyzed them on a single-cell level. For each receiving cell of a given cell type, we multiplied the log-normalized expression of the receptor with the average of the log-normalized expression of the ligands expressed by all cells of the corresponding sending cell type in a 50 μm radius (416.5 pixels). To limit the analysis to only RL pairs that did indeed spatially co-occur, we required at least 10% of the receiver cells to express both the receptor and be exposed to neighboring ligands. When this condition was not met, we excluded the RL pair from downstream analysis.

Cell type reference

The 2020 10X Genomics scRNA-seq dataset for the mouse whole cortex and hippocampus was downloaded from the Allen Brain Atlas Institute webpage. For analysis, a subset of the data was generated to only include regions annotated for 'RSP', 'TEa-PERI-ECT', 'ACA', 'AI', 'SSs-GU-VISC-AIp', 'AUD', 'MOp', 'MOs_FRP', 'PL-ILA-ORB', 'PTLp', 'SSp', 'VIS', 'VISl', 'VISm', 'VISp', 'HIP'. The remaining cells were randomly sampled to retain 12.5% of the cells (131,169 total cells). Wilcoxon rank-sum test, with multiplicity correction using the Benjamini-Hochberg (BH) method, was used to obtain the top 200 markers for annotated cell types (Glutamatergic neurons, GABAergic neurons, microglia, astrocytes, endothelial, and oligodendrocytes).